# Admission Thesis

submitted to the
Combined Faculties of the Natural Sciences and Mathematics
of the Ruperto-Carola-University of Heidelberg, Germany
for the admission to
a PhD programme

Put forward by
M.Sc. Florian Trost
born in Hagen

# Pulse Duration Measurement at FLASH2 by Intensity Autocorrelation in Neon and Argon

**Abstract**

For the first time, the duration of the extreme ultraviolet light pulse of the free-electron laser (FEL) FLASH2 at DESY, Hamburg, was measured by intensity autocorrelation. The FEL pulses were geometrically split into two replica which were focused into a gas target with a variable delay. The delay-dependent multiphoton ionisation rates of neon and argon represent the intensity autocorrelation of the FEL pulses from which the average pulse duration was determined. The ion rates were detected with a reaction microscope at the permanent user end station at beamline FL26. The measured FEL pulse durations range from $(32.4 \pm 2.4)$ fs to $(92.6 \pm 11.9)$ fs. Hence, these measurements represent the first benchmark of FLASH2 to routinely deliver intense extreme ultraviolet pulses in the femtosecond regime.

**Zusammenfassung**

Zum ersten Mal wurde die Pulslänge der extrem-ultravioletten Strahlung des Freie-Elektronen-Lasers (FEL) FLASH2 am DESY in Hamburg mittels Intensitäts-Autokorrelation gemessen. Die FEL-Pulse wurden geometrisch in zwei identische Teile aufgespalten und mit einem variablen Zeitunterschied auf einen Gasjet fokussiert. Die Multiphoton-Ionisationsraten von Neon und Argon repräsentieren die Intensitäts-Autokorrelationssignale der FEL-Pulse, aus welchen die Pulslänge bestimmt wurde. Die Ionisationsraten wurden mit einem Reaktionsmikroskop gemessen, welches Teil des permanenten experimentellen Aufbaus an Beamline FL26 ist. Die gemessenen Pulslängen liegen zwischen $(32.4 \pm 2.4)$ fs und $(92.6 \pm 11.9)$ fs. Diese Messungen sind der erste Nachweis dafür, dass FLASH2 routinemäßig Pulse im extrem-ultravioletten Spektrum im Femtosekundenbereich erzeugt.

# Contents

# 1 Introduction

When studying molecular quantum systems, measuring the initial and final state of their transitions can give some information on the systems' properties. To gain deeper insight into the underlying dynamics, however, it is desirable to also measure the molecules' intermediate states during the transition. In order to follow this temporal evolution, one must have a measure available shorter than the duration of the transition one wants to observe. Molecular motion such as dissociation and vibration happens on the femtoseconds time scale (Schnorr, 2014). In this regard, ultrashort laser pulses are a well-suited tool to investigate such dynamics on their natural time scale.

Pump-probe experiments are the most distinguished method for measuring the intermediate states and therefore the temporal evolution of molecular systems. The first pulse, called the "probe" pulse, initiates a reaction in the target. After some time of free temporal evolution, the second pulse, called "probe" pulse interacts with the target which results e.g. in dissociation of the system to be studied. By detecting the fragments in a reaction microscope by recoil-ion momentum spectroscopy, it is possible to obtain information on the system at the moment of dissociation. Examples for such molecular reactions are the proton transfer between water dimers and the time-resolved measurement of vibrational modes in diiodomethane ($CH_2I_2$), both conducted with the same user endstation at the Free-Electron Laser in Hamburg (FLASH2).

The recent development in free-electron lasers (FEL) which routinely deliver ultrashort pulses from the extreme-ultraviolet (XUV) to the X-ray regime made it possible to study molecular systems under far less perturbing conditions than with for example high intensity infrared lasers. The high intensity of FEL radiation compared to high-harmonic generation (HHG) also enables the study of nonlinear effects in multiphoton absorption processes in the XUV spectrum.

Since the temporal resolution of the pump-probe method is on the order of the laser pulse duration, it is crucial for the interpretation of the experimental results to know the pulse duration. There exist several methods of measuring FEL pulse durations, e.g. the detection of autocorrelation signals of the pulses (Yamanouchi and Midorikawa, 2012), measuring energy spectra of photoelectrons via IR streaking (U. F. *et al*, 2009), or inferring information on the pulse length from the longitudinal dimension of the electron bunches which created the FEL radiation (DESY, 2017a).

During this work, the pulse durations of FLASH2 at DESY, Hamburg, were measured via intensity autocorrelation since this direct method is easily implemented at the reaction microscope setup of beamline FL26. The rate of nonlinear multiphoton ionisation processes of noble gases represents the autocorrelation signal of the FEL pulse. From the features of the measured autocorrelation signals the average FEL pulse length can be determined. The results are the first experimental proof of FLASH2 being able to provide pulses of femtosecond duration at intensities high enough for XUV-XUV pump-probe experiments.

This thesis is structured as follows: In Section 2, the principles of creating ultrashort XUV pulses by FELs are discussed with a subsequent introduction to multiphoton ionisation processes. It follows an explanation on how FEL pulse durations can be determined from autocorrelation measurements. Section 3 describes the experimental setup at FLASH2 including the operational parameters of the FEL. The determination of the average FEL pulse durations is presented in Section 4. In Section 5 the conclusion of the measurements conducted during this work are summarised.

# 2 XUV Laser Pulses

The two predominant methods to create laser pulses in the extreme ultraviolet (XUV) range are high harmonic generation (HHG) and free-electron lasers (FEL). They differ in properties of the created radiation such as intensity and pulse length as well as in the dimensions of the necessary experimental setup. Both HHG and FELs create sufficiently short pulses to make pump-probe experiments feasible (A. L. C. *et al*, 2007; K. S. *et al*, 2013).

In HHG, the XUV radiation is created by focusing a high intensity infrared laser onto a nonlinear medium, e.g. a gas cell filled with argon (S. J. G. *et al*, 2015). Photoelectrons are created from atoms in the target. If a photoelectron is created at the right phase of the electric field of the laser, it follows a periodic trajectory and returns to its mother ion (see Fig. 1) with an increased kinetic energy of a maximum of $E_{\max} = 3.17U_p$ (Corkum, 1993). Here,

$$U_p = \frac{e^2}{8\pi^2\epsilon_0 c^3 m_e} I\lambda^2 \tag{1}$$

is the ponderomotive potential of a laser field of intensity $I$ and wavelength $\lambda$ (Hertel and Schulz, 2015, p. 438). If the electron recombines with the ion (ionisation potential $W_I$), a photon of energy up to

$$\hbar\omega_{HHG} = 3.17U_p + W_I \tag{2}$$

is emitted. HHG radiation with wavelengths down to a few nanometers and pulse durations of less than 70 attoseconds has been reported (K. Z. *et al*, 2012). The intensity of the created XUV radiation is much smaller than the intensity of the applied IR pulse because the conversion efficiency ranges from $\sim 10^{-7}$ to $\sim 10^{-5}$ (P. R. *et al*, 2013). HHG sources are available as table top devices which is very convenient compared to FELs that require large-

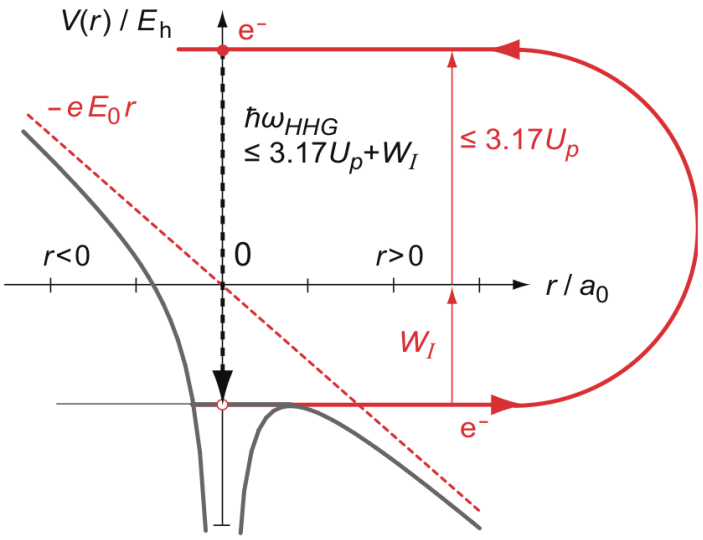


Figure 1: Schematic view of the HHG process. The back-scattered photoelectron has a kinetic energy of at maximum $3.17U_p$ which, in addition to its ionisation potential $W_I$, is available for generating high harmonics. From Hertel and Schulz, 2015, p. 439.

scale facilities (e.g. LCLS $>$ 3 km; Bozek, 2009). However, FEL radiation has the advantage of much higher XUV and X-ray intensities ($10^{18}$ W cm$^{-2}$ at LCLS; Bozek, 2009) compared to HHG radiation ($10^{14}$ W cm$^{-2}$; Mashiko, 2004). The FEL laser pulse durations measured during this work are in the order of tens of femtoseconds and therefore much longer than the shortest pulses currently achievable with HHG sources. However, their superior intensity makes FELs the preferred tool for XUV-pump-XUV-probe measurements.

## 2.1 Generation of femtosecond XUV Pulses with FELs

When charged particles are accelerated, they emit electromagnetic radiation. There are several examples of this effect in nature as well as in artificial applications. High energy electrons interacting with matter, e.g. the atomic

nuclei of a solid, decelerate and emit bremsstrahlung (Demtröder, 2009a, Ch. 7.5). The electrons can for example originate from radioactive $\beta$-decay. In X-ray scanners an electron beam is deliberately accelerated onto a solid metal anode to create X-rays for medical imaging (Hertel and Schulz, 2015, Ch. 10.6.1).

When the trajectory of fast electrons is changed by a bending magnet, they emit synchrotron radiation. In synchrotrons, the electrons' velocity is close to the speed of light which results in concentration of the emitted radiation in a narrow cone tangential to the electrons' path. This synchrotron radiation has a broad continuous frequency distribution from infrared to X-rays (R. W. S. *et al*, 2010). The pulse duration of tens of picoseconds depends on the length of the stored electron bunches, as described by R. W. S. *et al* (2010): "The time structure of the temporally incoherent synchrotron radiation is directly determined by the time structure of the electron bunch and is invariant over the entire spectrum of the synchrotron emission [...]".

FELs use the creation of radiation from accelerated electrons in undulators. An undulator is a periodic arrangement of dipole magnets with alternating polarity. The undulator period $\lambda_u$ is the distance between two magnets with equal polarity. This creates a transverse alternating magnetic field along the electrons' direction of motion. In a planar undulator (see Fig. 2) electrons are forced onto sinusoidal trajectories which results in the emission of linearly polarised radiation (Schmüser, Dohlus, and Rossbach, 2008, Ch. 2.3). There is also the possibility of creating circularly polarised radiation by using helical undulators as described by Pellegrini (2016b). This process is, however, not further addressed in this work and from now on only the planar type is meant when mentioning undulators. The following summary of the physical processes that lead to the creation of FEL radiation is compiled from Schmüser, Dohlus, and Rossbach (2008) and Pellegrini (2016a).

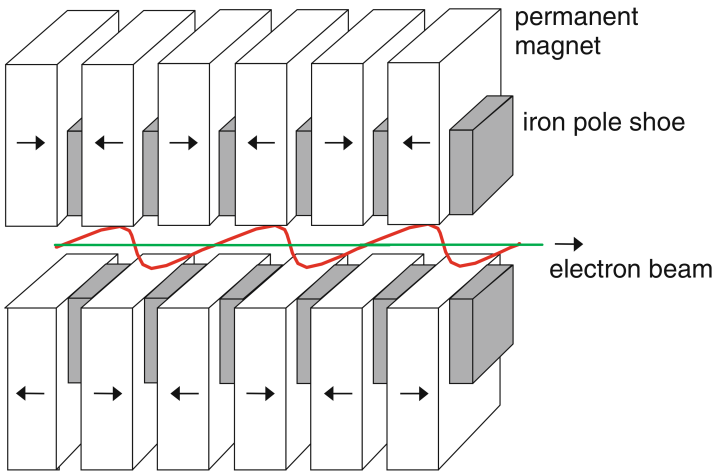


Figure 2: Schematic of the magnet arrangement of a planar undulator. The amplitude of the sinusoidal electron trajectory is exaggerated. From Schmüser, Dohlus, and Rossbach, 2008, p. 11.

Due to relativistic length contraction, the undulator period in a coordinate frame moving with the electrons is smaller than in the rest frame, $\lambda_u^* = \lambda_u/\gamma$. The Lorentz factor $\gamma$ is directly related to the total relativistic energy $W$ of the electrons, $\gamma = W/m_e c^2$.
The fundamental wavelength of the radiation emitted by electrons in an undulator in forward direction is therefore approximately

$$\lambda_l \approx \frac{\lambda_u^*}{2\gamma} = \frac{\lambda_u}{2\gamma^2} = \frac{m_e c^2}{2}\frac{\lambda_u}{W^2}. \tag{3}$$

Both the undulator period and the total electron energy influence the photon wavelength. Additionally, the strength of the magnetic field of the undulator affects the fundamental wavelength through the undulator parameter $K = eB_0\lambda_u/2\pi m_e c$ where $e$ is the elementary charge, $m_e$ the electron mass, and $c$ the speed of light. $B_0$ is the maximum value of the magnetic field strength along the undulator axis. A more refined expression for the fundamental

wavelength of the undulator radiation is (Schmüser, Dohlus, and Rossbach, 2008, p. 17)

$$\lambda_l = \frac{\lambda_u}{2\gamma^2}\left(1 + \frac{K^2}{2}\right) \quad \text{with} \quad K = \frac{eB_0\lambda_u}{2\pi m_e c}. \tag{4}$$

The wavelengths achievable with FELs lie far below what is currently possible with conventional lasers and ranges down to the hard X-ray regime. Because the FEL method of light creation is not bound to any fixed energy levels in quantum systems a continuous band of wavelengths is accessible. When using variable gap undulators, such as FLASH2 at DESY, Hamburg, the FEL wavelength can be adjusted without changing the electron beam energy. This enables wavelength changes within seconds after user request.

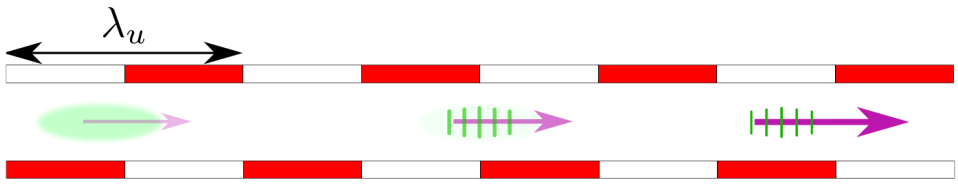


Figure 3: An electron bunch travelling through an undulator is split up into individual microbunches. From Schnorr, 2014, p. 42.

In the FEL process, first an electrode is irradiated with a pulsed laser to create photoelectron packages. The electrons are subsequently accelerated to relativistic energies. Then, the electron bunches enter an undulator and emit electromagnetic radiation as a result of their transverse deflection. Depending on the phase between the electrons' trajectory and the wave of the FEL radiation, there is different energy transfer between the electrons and the light field. This results in electrons losing or gaining longitudinal velocity and concentrating in microbunches (see Fig. 3). The distance between microbunches is on the order of the FEL wavelength, but the microbunches themselves are longitudinally much smaller than their distance. One mi-

crobunch consisting of $n_e$ electrons oscillates like a single particle of charge $-en_e$. "This leads to correlated emission of radiation, which is fully coherent within one microbunch." (Schnorr, 2014, p. 42). There is however no coherence between the radiation emitted from different microbunches, hence the term partial coherence is used to describe FEL radiation. Because of microbunching the radiation power of FELs scales quadratically with the number of electrons in each microbunch which makes them unique compared to other sources of undulator radiation such as synchrotrons.

The starting point of the microbunching process can be initiated by external seed radiation or by so-called self-amplified spontaneous emission (SASE). A seeded FEL has the advantage of increased stability in output power as well as spectral and temporal pulse properties. Seeding radiation with the necessary characteristics such as tunability and sufficient power is not readily available in the XUV and X-ray energy range. HHG sources are a promising source of direct seeding radiation, but yet lack the required intensity (Pellegrini, 2016a). SASE is caused by a periodic charge density modulation in the electron beam that leads to spontaneous emission when the electron bunches enter the undulator. Because this initial distribution is slightly different for every electron bunch, the SASE-created FEL pulses exhibit a per-shot fluctuation in energy as well as spectral and temporal flux.

Currently there exist several FELs in the world. FLASH at DESY started user operation in 2005 and has since then been upgraded with a second undulator and several additional beamlines in the FLASH2 experimental hall. FLASH2 started user operation in 2016. The Linac Coherent Light Source (LCLS) at the SLAC National Accelerator Laboratory in Menlo Park, California, USA, provides FEL radiation down to sub-nanometer wavelengths since 2009 (A. L. *et al*, 2016). FERMI in Trieste, Italy, is a seeded FEL that produces highly tunable coherent laser pulses (FERMI, 2017). The currently youngest facility is the SwissFEL which had its inauguration on 05 Decem-

ber 2016 (SwissFEL, 2017). Other FELs exist in Japan (SCSS, SACLA), South Korea (PAL-XFEL), and Shanghai (SDUV-FEL). Another new facility, the European X-ray free-electron laser (European XFEL) is currently being constructed in Hamburg and first user experiments are scheduled for 2017 (XFEL, 2017).

## 2.2 Multiphoton Ionisation with XUV Radiation

The response of an atom to electromagnetic radiation strongly depends on the photon energy. Examples of processes that can be induced are, with increasing energy: elastic Rayleigh scattering, inelastic photoionisation, Compton scattering, and pair creation (Demtröder, 2009b, Ch. 4.3.2). During this work photon energies of a few dozen electronvolt (eV) are considered. In this energy range photoionisation is the dominant process upon interaction.

The absorption of one or more photons by an atom initiates a transition from an initial to a final state. The final state can either be a bound state (photoexcitation) or a continuum state (photoionisation), as shown in Fig. 4. In a photoionisation process the created photoelectron has a kinetic energy $E_{\mathrm{kin}}$ corresponding to the excess energy of the photon $E_\nu = \hbar\omega$ above the electron's binding energy $W_I$:

$$E_{\mathrm{kin}} = \hbar\omega - W_I. \tag{5}$$

If the energy difference between the initial and the final state of the system is larger than the photon energy, the transition cannot happen with the absorption of only one photon. The absorption of multiple photons can, however, initiate the process if the combined energy of the photons is larger than the energy difference (M. L. *et al*, 1973). Two cases must be distinguished here: sequential (or direct) and non-sequential multiphoton processes. For simplicity, the following consideration is reduced to a two-photon ionisation process.

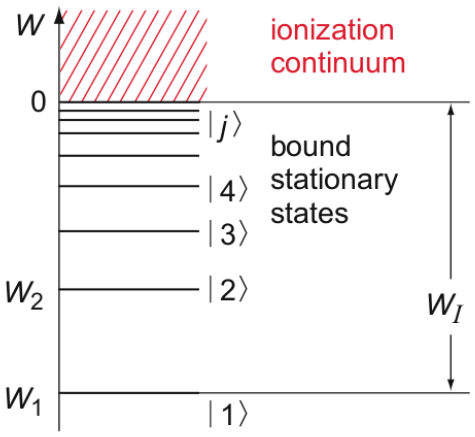


Figure 4: General electronic energy levels of an atom with ionisation potential $W_I$. When an electron receives enough energy to reach the ionisation continuum, it is no longer bound and the atom is ionised. From Hertel and Schulz, 2015, p. 177.

If the intermediate state between the absorption of the first and the second photon is an energy eigenstate of the atom, its lifetime is rather long compared to the applied ultrashort laser pulse. It is therefore possible for the atom to first absorb one photon, reach the intermediate state and, after some time, absorb a second photon for photoionisation. This is called the sequential process. It is for example observed in a resonant $2p-3s$ excitation in $Ne^+$ ions at 27.2 eV (45.6 nm), see Fig. 5. The energy of the photons (represented by the vertical arrows) in the diagram is tuned to the resonance of the $2p-3s$ excitation. A $Ne^+$ ion in the ground state absorbs a photon and is excited to the $Ne^+$ $2s^2 2p^4 3s$ state. After some time, it absorbs a second photon (arrow on the top right in the diagram) and emits a second photoelectron, reaching the ground state of $Ne^{2+}$.

The two-photon ionisation process can, however, also happen if there is no resonant excitation into a stationary intermediate state (L. A. L. *et al*, 1977; Gontier and Trahin, 1971). If the atom absorbs the second photon during

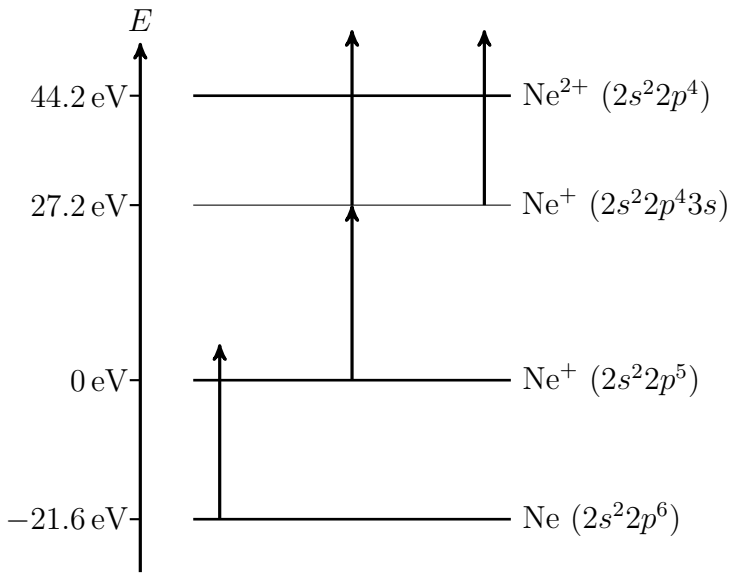


Figure 5: Term diagram of double ionisation of neon. Photon energy is on $2p - 3s$ resonance at 27.2 eV. First, the neon atom is ionised to the $Ne^+$ ground state by the absorption of one photon. The second ionisation to $Ne^{2+}$ is a two-photon process. It can happen either direct (subsequent arrows in the centre) or sequential. In the sequential case, the energy level $Ne^+$ $2s^2 2p^5 3s$ is excited by one photon and, after some time, a second photon ionises the excited ion to the $Ne^{2+}$ ground state.

the very short lifetime of this virtual state, the transition to the final state can occur (subsequent arrows in the centre of Fig. 5).

The transition rate of a process depends on how many photons participate in the transition. For a simple single-photon absorption that transfers atoms from their ground state (a) to an excited or ionised state (b), the excitation rate depends linearly on the laser intensity, as described by Hertel and Schulz, 2015, Ch. 4.2.3. The laser intensity

$$I = c\hbar\omega N_{ph} \tag{6}$$

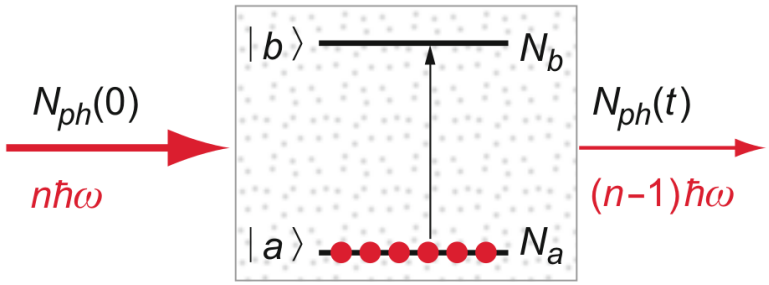


Figure 6: Schematic view of a laser beam with photon density $N_{ph}$ crossing a medium. The atoms of the medium have two discrete energy states: the ground state (a) and the excited state (b). The photons interact with the atoms and excite them from (a) to (b), changing the populations $N_a$ and $N_b$. From Hertel and Schulz, 2015, p. 179.

decreases exponentially upon interaction with a medium. Here $\hbar\omega$ is the photon energy, $c$ is the speed of light, and $N_{ph}$ is the photon density (number of photons per volume). Since the absorption of a photon increases the number of excited atoms by one and reduces the number of photons by one (Fig. 6), the intensity is connected with the excitation rate (adapted from Hertel and Schulz, 2015, p. 179):

$$\frac{dN_a}{dt} = \frac{dN_{ph}}{dt} = \frac{1}{c\hbar\omega}\frac{dI}{dt} = \frac{1}{\hbar\omega}\frac{dI}{dz} = -N_a\sigma\frac{I}{\hbar\omega} \tag{7}$$

Here, $\sigma_a$ is the cross section of state (a) which influences the probability that an excitation happens.

The consideration of a three-state system consisting of the ground state (a), an excited state (b), and a further excited state (c) can give insight into the intensity dependence of sequential multiphoton processes. It is assumed that both transitions (a) to (b) and (b) to (c) can happen by single-photon absorption. No direct transition (a) to (c) is possible and decay of the excited states (b) and (c) is neglected. The populations of states (a), (b), and (c)

are called $N_a$, $N_b$, and $N_c$ with their respective cross sections $\sigma_a$, $\sigma_b$, and $\sigma_c$. Then, the changes in state populations are

$$\frac{dN_a}{dt} = -N_a\sigma_a\frac{I}{\hbar\omega} \tag{8}$$

$$\frac{dN_b}{dt} = -\frac{dN_a}{dt} - N_b\sigma_b\frac{I}{\hbar\omega} \tag{9}$$

$$\frac{dN_c}{dt} = N_b\sigma_b\frac{I}{\hbar\omega} \tag{10}$$

Solving Eqn. 8 for $N_a$ results in the expected exponential decay of the population of state (a):

$$N_a(t) = N_{a0}e^{-\sigma_a\frac{I}{\hbar\omega}t} \tag{11}$$

Using this in the differential equation for $N_b$ gives

$$N_b(t) = N_{a0}\frac{\sigma_a}{\sigma_a - \sigma_b}\left(e^{-\sigma_b\frac{I}{\hbar\omega}t} - e^{-\sigma_a\frac{I}{\hbar\omega}t}\right). \tag{12}$$

With this result, the change in population of state (c) can be written as

$$\frac{dN_c}{dt} = N_b\sigma_b\frac{I}{\hbar\omega} = N_{a0}\frac{\sigma_a\sigma_b}{\sigma_a - \sigma_b}\frac{1}{\hbar\omega}\left(e^{-\sigma_b\frac{I}{\hbar\omega}t} - e^{-\sigma_a\frac{I}{\hbar\omega}t}\right)I. \tag{13}$$

By Taylor-expanding the exponential parts and assuming low intensity, higher-order terms can be neglected and the resulting change in population of state (c) is approximately

$$\frac{dN_c}{dt} \approx N_{a0}\frac{\sigma_a\sigma_b}{\sigma_a - \sigma_b}\frac{1}{\hbar\omega}\left(1 - \sigma_b\frac{I}{\hbar\omega}t - 1 + \sigma_a\frac{I}{\hbar\omega}t\right)I \tag{14}$$

$$= N_{a0}\sigma_a\sigma_b\frac{1}{(\hbar\omega)^2}I^2t \tag{15}$$

$$\propto I^2 \tag{16}$$

This shows that, for small intensities, the overall transition rate from state (a) to state (c) via two sequential single-photon absorptions has a quadratic

dependence on intensity. The same result is found when applying quantum mechanical time-dependent perturbation theory as was summarised by Schnorr (2014). In general, for an $n$-photon absorption process the transition rate $R_d^{(n)}$ scales with the laser pulse intensity $I$ to the power of $n$ (Schnorr, 2014):

$$R_d^{(n)} \propto I^n \tag{17}$$

This allows to identify the order of a photoionisation process by measuring the intensity dependence of the ion yield. Additionally, changes in the ionisation rate can give information on variations of the laser intensity. This principle is used in this work to measure the duration of FEL laser pulses as described in detail in the next section.

## 2.3 Pulse Duration Measurement of femtosecond XUV Laser Pulses

There exist several methods of measuring the duration of FEL laser pulses. The three most often used methods are intensity autocorrelation and cross-correlation (Yamanouchi and Midorikawa, 2012; R. R. *et al*, 2013), terahertz streaking (U. F. *et al*, 2009), and inferring the laser pulse duration from the longitudinal extension of the electron bunches (at FLASH with LOLA; DESY (2017a)). It is also possible to deduce properties of the temporal structure from the number of longitudinal modes of the FEL radiation and the spectral shape of the pulses (V. A. *et al*, 2006). However, autocorrelation and terahertz streaking are methods of higher accuracy.

At FLASH, single-shot terahertz (THz) streaking has been applied to soft X-ray pulses by U. F. *et al* (2009). Photoelectrons are created by interaction of an FEL pulse with a gaseous target. A superimposed THz pulse creates the streaking field. The photoelectrons created by the leading edge of the FEL pulse experience a slightly different electric field caused by the THz pulse

than the electrons created by the trailing edge. The result is a broadening in the kinetic energy spectrum of the photoelectrons. It is therefore possible to reconstruct temporal features of the FEL pulse from the measured kinetic energy spectrum (U. F. *et al*, 2009, Fig. 6).

Because the creation of the photoelectrons depends on the ionisation process of a gaseous target, terahertz streaking is applicable only in a limited wavelength range (R. R. *et al*, 2013). Additionally, a dedicated experimental setup and precisely synchronised THz streaking pulses are required. This makes terahertz streaking a rather demanding technique for obtaining information on the temporal structure of FEL pulses. The measurement of the pulse duration at FLASH during this work was done via intensity autocorrelation in ionisation rates of noble gases. This method only provides average values for pulse durations, but it is easier to implement at the present experimental setup (see Section 3).

### 2.3.1 Intensity Autocorrelation

R. R. *et al* (2013) measured the FEL pulse duration at FLASH via the change in transient reflectivity of a solid material. The absorption of the FEL pump pulse increases the electron density in the material which in turn reduces its transmission rate for an optical probe pulse. By varying the delay between the pump and probe pulses and measuring the intensity of the transmitted optical pulse one obtains the cross-correlation

$$S(\delta) = \int_{-\infty}^{\infty} I_{\mathrm{Laser}}(t) G(I_{\mathrm{FEL}}(t-\delta)) dt \tag{18}$$

with $I_{\mathrm{Laser}}$ being the intensity of the probe pulse and $G$ as the gating function that relates the transmission of the material to the FEL pulse intensity (R. R. *et al*, 2013, p. 3).

During this work however, not the cross-correlation of two different pump and probe pulses but of one single pulse split into two parts was measured. The cross-correlation of a function with itself is called autocorrelation. Each incoming FEL pulse was split (see Section 3) and both parts were focused onto the target with a well-defined variable delay $\delta$. Then, the detected ion counts depending on the delay between the pulses represents the autocorrelation function. The order $n$ of the autocorrelation is determined by the intensity dependence of the ionisation process (see Section 2.2) as described by Yamanouchi and Midorikawa (2012) for second-order ionisation processes:

$$A^2(\delta) = \int_{-\infty}^{\infty} I(t)I(t-\delta)dt \tag{19}$$

It is often assumed that FEL pulses have a Gaussian-shaped intensity envelope (T. P. *et al*, 2010; R. R. *et al*, 2013). Following this assumption, the second-order autocorrelation of a Gaussian function with standard-deviation $\sigma_p$ is itself a Gaussian function with larger standard deviation $\sigma_{ac}$ (Bromiley, 2014):

$$\sigma_{ac,2} = \sqrt{2}\sigma_p \tag{20}$$

The width of the autocorrelation function of a second-order ionisation process therefore contains information about the width of the original pulse intensity profile. According to Yamanouchi and Midorikawa (2012), the standard deviation of a third-order autocorrelation signal as they measured for the three-photon ionisation of $Ar^{3+}$ to $Ar^{4+}$ has a standard deviation a factor of $\sqrt{3/2}$ larger than the original pulse intensity:

$$\sigma_{ac,3} = \sqrt{\frac{3}{2}}\sigma_p \tag{21}$$

A typical way of comparing widths of signals is by the full width at half maximum (FWHM). For a Gaussian function, the FWHM depends on the standard deviation in the following way:

$$
\begin{aligned}
y(t_{\mathrm{FWHM}}) &= C\ exp\left(-\frac{t_{\mathrm{FWHM}}^2}{2\sigma^2}\right) = \frac{1}{2}\ C && (22)\\
&\Rightarrow\ -\frac{t_{\mathrm{FWHM}}^2}{2\sigma^2} = \ln\left(\frac{1}{2}\right) = \ln(1) - \ln(2) = -\ln(2) && (23)\\
&\Rightarrow\ t_{\mathrm{FWHM}} = \sqrt{2\ln(2)}\ \sigma && (24)\\
&\Rightarrow\ \mathrm{FWHM} = 2\ t_{\mathrm{FWHM}} = 2\sqrt{2\ln(2)}\ \sigma && (25)
\end{aligned}
$$

From now on, when the duration of an FEL pulse is mentioned, always the FWHM of its intensity profile is meant, if not specified otherwise. It is important to distinguish the pulse length from another feature of the FEL pulse which is represented in the autocorrelation signal: a sharp spike at approximately zero delay which is connected to the partial coherence of the FEL pulses, as discussed in the next section.

### 2.3.2 Partial Coherence Method for FEL Pulse Simulation

Some FEL parameters can be determined on a per-shot basis, for example the spectral shape via the Online Photoionisation Spectrometer (OPIS) at FLASH (DESY, 2017c). The pulse duration however is usually not provided as a readily available parameter during FEL operation. Elaborate and/or time-consuming measurements are necessary to obtain information on the FEL pulse duration which is, at least in part, the reason for the relative scarcity of data on that topic. In order to obtain input for computational simulations, the partial-coherence method (PCM) as described by T. P. *et al* (2010) has been developed. Starting from knowledge of average FEL pulse parameters such as average spectral shape and duration, this method simulates individual temporal intensity profiles of FEL pulses. Because the partial coherence properties of FEL radiation are included in the simulation, the autocorrelation of the resulting simulated pulses shows a coherence feature centred around zero delay. This coherence spike was found in most of the measurements taken during this work and it is therefore important to

understand its origin. The following description is summarised from T. P. *et al* (2010).

Starting from the average spectrum of the FEL pulses $I(\omega)$ one defines the electric field in the frequency domain via a discrete spectral amplitude and a discrete random spectral phase function $\phi_0$:

$$E(\omega_i) = A_0(\omega_i) \exp\left(i\phi_0(\omega_i)\right) \tag{26}$$

with

$$A_0(\omega_i) = \sqrt{I_0(\omega_i)} \tag{27}$$

Here the density of the discrete sampling values $\omega_i$ depends on the measured average pulse duration $\tau$:

$$|\omega_i - \omega_{i+1}| \ll \frac{2\pi}{\tau} \tag{28}$$

The spectral electric field is Fourier transformed into the time domain and multiplied by a temporal filtering function $F_0(t)$. This filtering function is chosen to represent the average temporal pulse shape of the FEL pulses, usually a Gaussian profile. By reverse Fourier transform of the filtered temporal electric field one obtains spectral structures of FEL pulses with partially constant phase, hence the name partial coherence method. Because one uses a random initial discrete spectral phase function the results are samples of different individual pulse shapes that, on average, represent the previously known FEL parameters.

T. P. *et al* (2010) show that the second-order autocorrelation function resulting from the sampled Gaussian FEL pulses indeed resembles a Gaussian function again. The observed broad base feature is influenced by the width of the applied filtering function $F_0(t)$ and therefore depends on the pulse

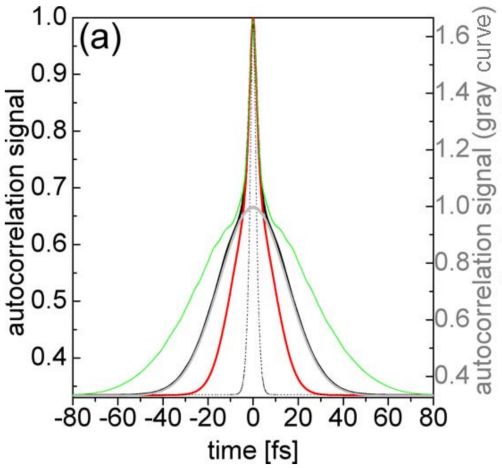


Figure 7: Average autocorrelation signals calculated with the partial-coherence method (green, black, and red curves). From T. P. *et al*, 2010.

duration. The sharp spike feature at zero delay emerges from the partial coherence of the individual laser pulses (see Fig. 7). These two features could be identified in the recorded autocorrelation signals of $Ne^{2+}$, $Ar^{2+}$, and $Ar^{4+}$ as presented in Section 4.

### 2.3.3 Autocorrelation of simulated Intensity Signals of FEL Pulses

This section describes a short proof-on-concept method for simulating a Gaussian intensity signal and calculating its FWHM from its autocorrelation signal. This offers a simple method of examining the expected results of an autocorrelation measurement and checking the method of extracting the original pulse duration from the measured signal. The method presented here is a less sophisticated procedure of generating individual FEL pulses than the PCM of T. P. *et al* (2010) described in Section 2.3.2 and does not take coherence properties into account, but it does work for the purpose of a simple demonstration. The code that generated the following examples can be reviewed in Appendix A.

A discrete time-domain signal is created by a Gaussian function with predefined parameters (scale, mean, and standard deviation). This shall represent the original temporal intensity distribution of an FEL pulse. To emulate real FEL pulses, a jitter function is applied to the Gaussian pulse shape. Because the jitter is created from random numbers, every simulated pulse looks different from previously generated ones. It should be noted that the actual pulse intensity profiles reconstructed e.g. from spectral properties look quite different (U. F. *et al*, 2009).

The autocorrelation of the generated intensity profile is computed and superposed with the original signal for comparison. Several of the generated pulses together with their respective autocorrelations are shown in Fig. 8. As expected, the autocorrelation functions of the Gaussian pulses have as well a roughly Gaussian shape. The sharp spike at zero delay, most of the time consisting of only one point, varies in prominence between pulses but is a distinct feature in all examined autocorrelation signals. This behaviour of the autocorrelation function is in accordance with expectation from T. P. *et al* (2010), even though the intensity profiles were created without taking into account their phase and the resulting partial coherence.

When using a nonlinear least squares method to fit a Gaussian function to the autocorrelation signal one obtains its standard deviation as a fit parameter. Then, the FWHM of the original pulses is calculated via Eqn. 25 and shown in each subfigure in Fig. 8. The original pulse had a standard deviation of $\sigma_p = 3$ and therefore $\mathrm{FWHM}_p = 7.064$. This simulation with subsequent autocorrelation analysis of intensity profiles is an indication that the measurement of autocorrelation signals can indeed give some insight into the duration of FEL pulses.

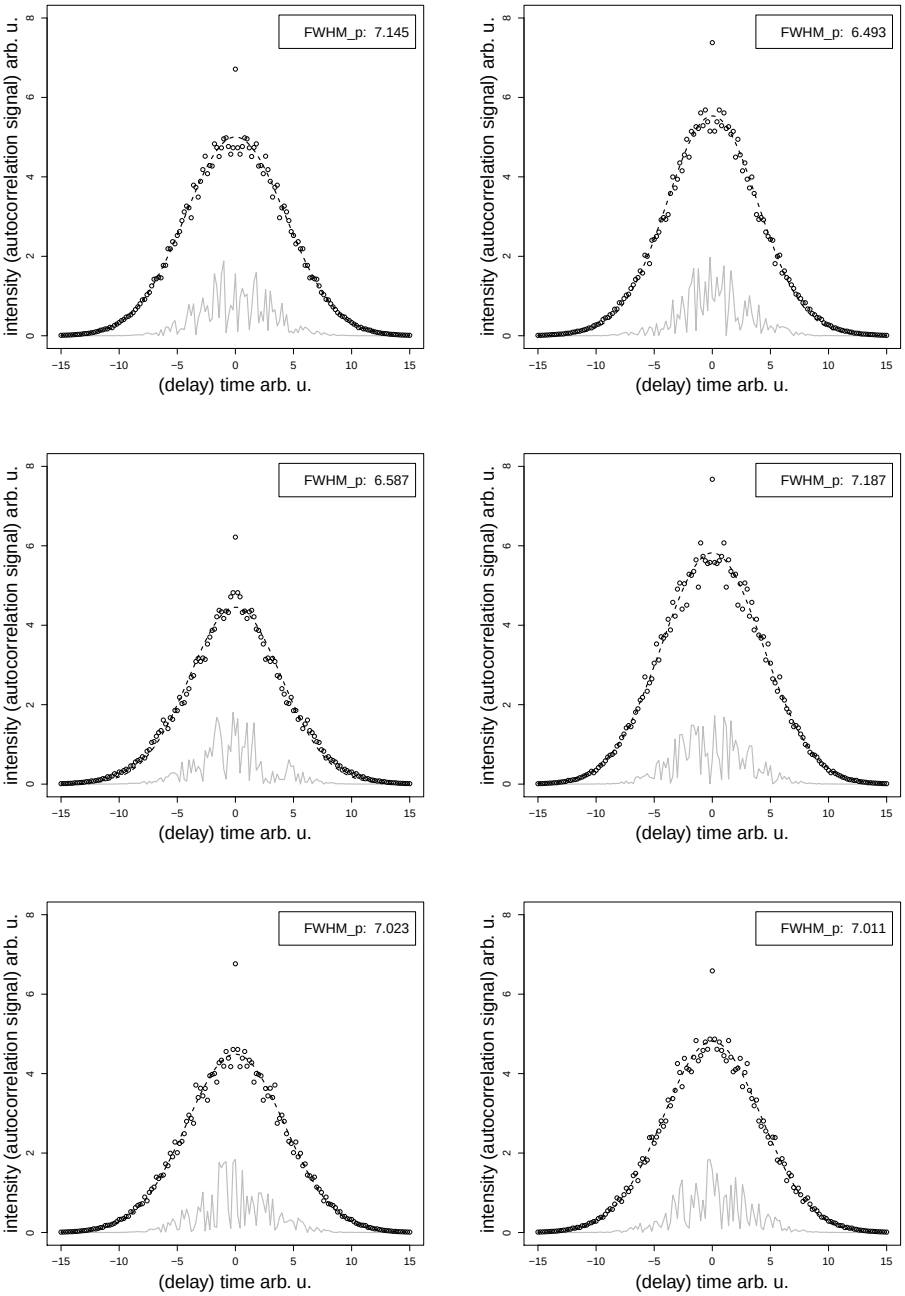


Figure 8: Simulated Gaussian pulse intensity profiles (grey bold line) superposed with their respective autocorrelation (black dots). A Gaussian fit (black dashed line) to the autocorrelation signals gives an estimate of the FWHM of the original pulses and is displayed in each subfigure. The pulses were simulated with a FWHM of 7.064 (standard deviation of 3).

# 3 Experimental Setup at FLASH

## 3.1 Reaction Microscope

This work is centred on pulse length measurements of the FEL radiation delivered by FLASH. Because the applied method does not take advantage of all features a reaction microscope (REMI) offers, only a brief description of all necessary parts is presented here. It has been compiled from the detailed technical records of Schnorr (2014) and R. M. *et al* (1996).

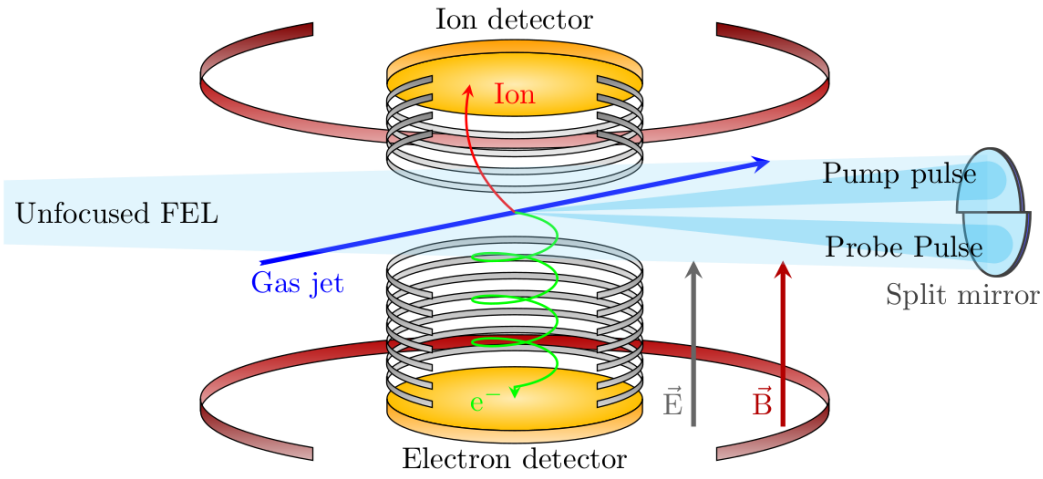


Figure 9: Schematic view of a reaction microscope for coincidence detection of all charged fragments from an atomic or molecular reaction. From Schnorr, 2014, p. 50.

The working principle of a REMI is to measure all charged fragments emerging from an atomic or molecular reaction in coincidence. In doing so, the time-of-flight (TOF) and the impact position on the detectors it is measured and the three-dimensional momentum vectors of all fragments are reconstructed. The general setup of a REMI with all functional parts is shown in Fig. 9. The charged particles created by ionisation of target atoms/molecules are accelerated by an electric field applied by a spectrometer. By varying the

electric field strength the solid angle of detection can be adjusted. With a strong enough electric field, a $4\pi$ solid angle of detection is achievable for the ions. The magnetic field is necessary to ensure a $4\pi$ acceptance for the much lighter electrons. However, the electrons were not detected during the experiments presented in this work and therefore no magnetic field was applied.

### 3.1.1 Back-reflecting Split Mirror

In order to perform pump-probe measurements it is necessary to split and delay the incoming FEL pulses by a precisely amount of time. These two tasks are performed by the back-reflecting split mirror. It resides in the mirror chamber on the opposite side of the REMI with respect to the incoming FEL beam. It consists of two half-circular mirrors separated by a horizontal gap that is visible in Fig. 10.

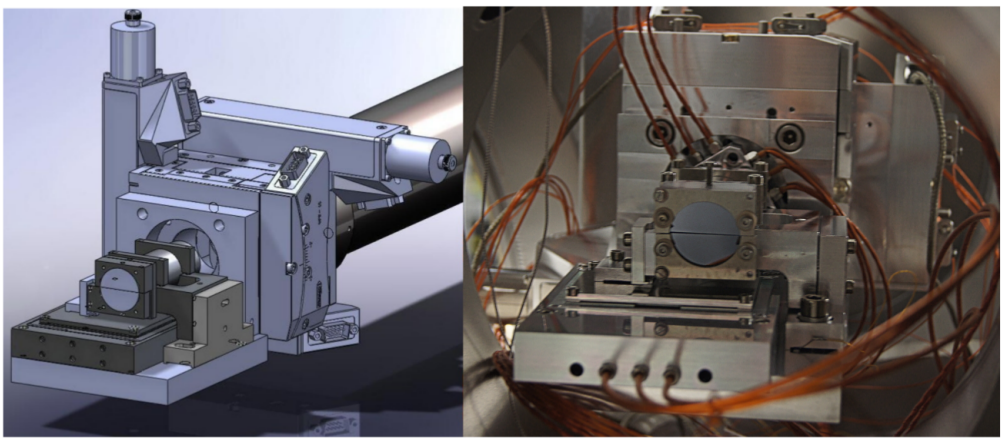

Figure 10: CAD drawing (left) and photograph (right) of the split mirror. The horizontal gap between the upper and lower part of the mirror is seen. From Schnorr, 2014, p. 71.

Each of the two mirrors focuses the respective part of the FEL beam into the target. The upper mirror part can be tilted with a piezo stage which allows to achieve overlap of the two foci in the target. With two goniometers, both mirror parts can be rotated as one piece to adjust the position of the overlapped foci. But most importantly, the mirrors can introduce a delay between the two reflected pulses. This is done by varying the path length of the lower FEL part with respect to the upper part. With a piezo-driven translation stage the position of the lower mirror is changed along the axis of the incoming beam. The maximum possible translation of 800 µm results in a maximum delay of 5.33 ps. The resolution of the mirror translation is sufficient to achieve a sub-femtosecond resolution in the delay (Schnorr, 2014, p. 71). The reflectivity of the mirror depending on the photon energy is shown in Fig. 11.

The incoming unfocused FEL beam crosses the main chamber once to hit the split mirror and is then focused into the target. In order to avoid previous interaction of the beam with the target, a thin wire is placed into the path of the beam before it enters the main chamber for the first time. This wire blocks a part of the FEL which is approximately in the diameter size of the jet. Therefore, the jet is in the "shadow" of the wire when the unfocused FEL crosses the main chamber.

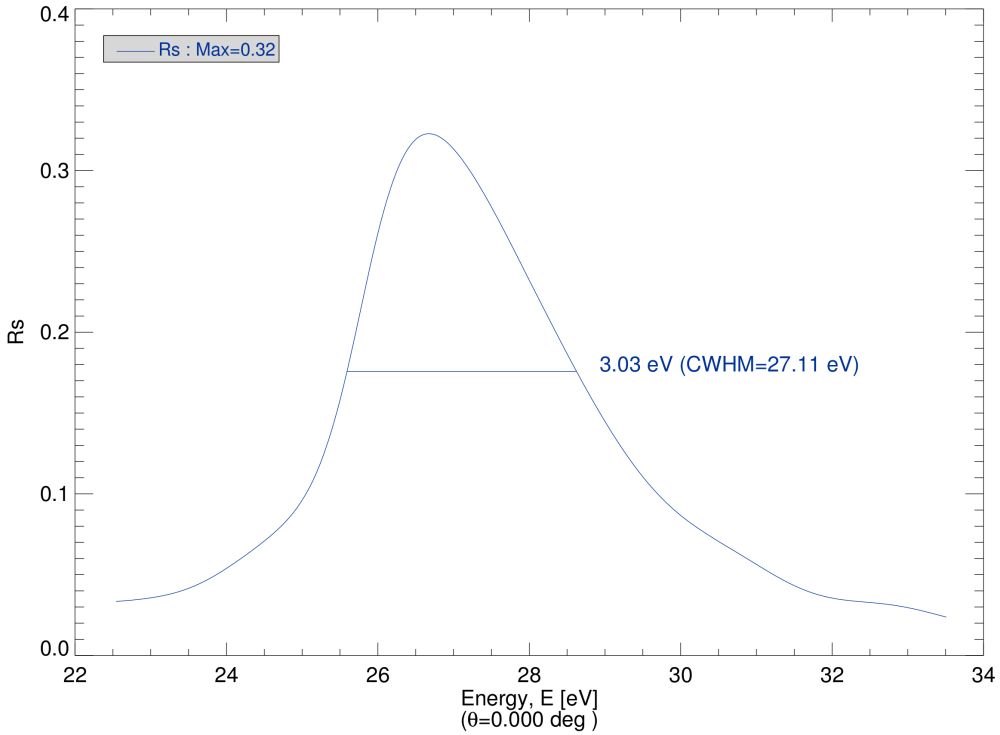


Figure 11: Reflectivity of the back-reflecting split mirror depending on the photon energy. From Feigl, 2017.

### 3.1.2 Jet Stage

The atomic target is prepared by supersonic expansion of a gas. Two different jet sources have been used during the measurements presented in this work. One of the sources has the capability to use liquids for target generation, alone or in combination with a gas. It was designed by Severin Meister, a detailed description of its function can be found in Meister (2016, Ch. 3). The other jet source was designed for gas targets only. Here, only a brief summary is given to explain its basic functionalities.

The gas jet is formed in the jet source and guided through several differentially pumped stages before it reaches the main chamber where it is exposed to the FEL radiation (see Fig. 12). It is necessary to separate the source

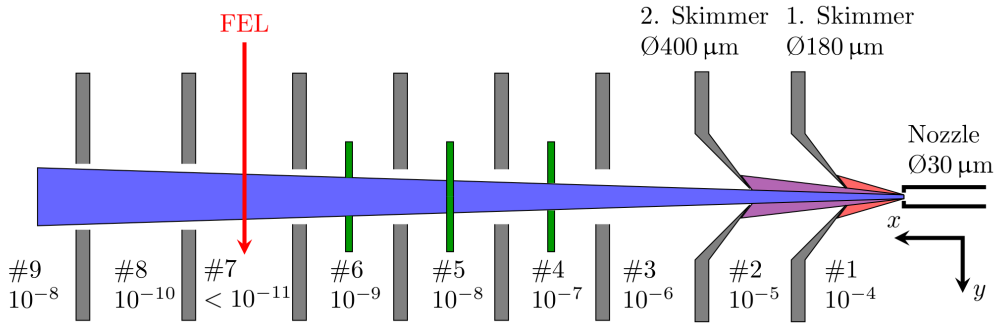


Figure 12: Schematic of the different jet stages between the source (#1) and the main chamber (#7) with their typical pressure values. Fractions of the jet containing atoms of higher transversal velocity are cut away by the skimmers. Through movable apertures (green) the dimension of the jet can be adjusted. From Schnorr, 2014, p. 53.

from the interaction zone with pumping stages to ensure the ultra-high vacuum conditions in the main chamber. The jet exits the main chamber on the opposite side and enters the jet dump where the jet is pumped away by turbomolecular pumps. As a result of passing through several skimmers and adjustable apertures, the gas jet is highly collimated when entering the main chamber. This minimises the dissipation of gas from the jet in the main chamber and further reduces the background pressure. A pressure reducing regulator allows for adjustment of the backing pressure in the source reservoir. The gas expands through a micrometer pore (between 30 to 50 µm) and gains supersonic velocity and low momentum divergence (Meister, 2016, Ch. 2.1).

### 3.1.3 Detectors

The two detectors at the opposite ends of the spectrometer measure the time and impact position of charged fragments (ions and electrons) resulting from a reaction. Since in this work only ions were measured, the focus lies on the description of the ion detector. First the time-of-flight from the interaction point to the detector is measured by a micro-channel plate (MCP). Afterwards, the electron cloud exiting the MCP triggers a delayline anode that measures the two-dimensional position of impact. The two parts of the detector are shown in Fig. 13.

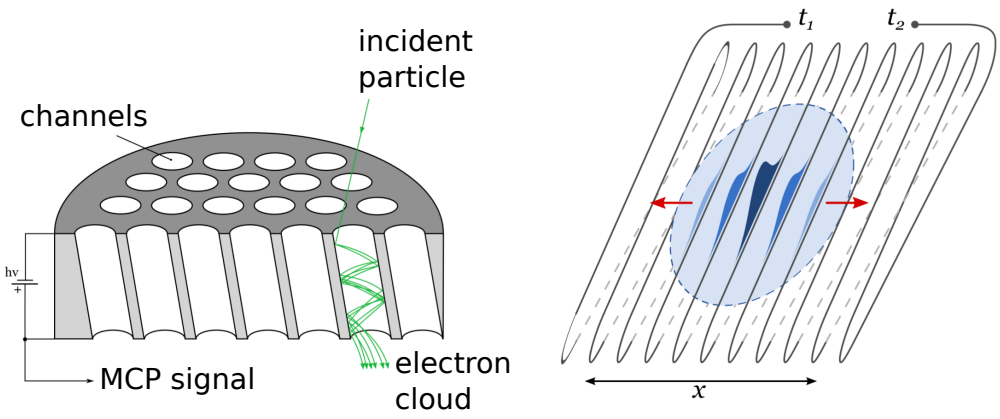


Figure 13: Schematic view of a microchannel plate (MCP) (left) and a delayline anode (right). The MCP measures the time-of-flight of impacting particles and creates a localised electron cloud. The delayline anode measures the position of the electron cloud by signal run-time differences resulting in two-dimensional spatial information of the original particle. From Meister, 2016, p. 61.

An MCP is a thin glass plate with a two-dimensional array of many small holes, called channels, each of which acts as an electron multiplier. The large electrical resistance of the plate material allows to apply a voltage of more than 2 kV along the channels. When a charged particle hits the inner surface of one of the channels, it creates secondary electrons which are accelerated

inwards by the applied voltage and more electrons are created. This charge avalanche can be detected as a short drop in the applied voltage which is converted into the time-of-flight of the particle. In order to reduce the probability of ions passing through the MCP without hitting a channel wall, the channels are tilted with respect to the surface normal by 8°. The gain is further increased by stacking several MCPs on top of each other which is usually done such that the combined channels form a V-shape, called chevron geometry. This geometry also reduced the probability of ion feedback from inside the channels. MCPs do not directly provide information on the impact position of a particle. However, the electron cloud exiting the MCP on its back side is localised to the position of impact and can be used as input to a position-sensitive delayline anode.

The delayline anode is a thin copper wire held at a positive potential with respect to the back side of the MCP (Schnorr, 2014, Ch. 4.1.3). The electron cloud from the MCP impacts the wire and creates a signal. The signal propagates along the wire in both directions and is detected at the two ends (see Fig. 13). From the difference in run-time of the signal the impact position is calculated. By using two insulated wires perpendicular to each other, the two-dimensional position information of the MCP electron cloud, and, therefore, of the original impacting ion is obtained. The sum of the two measured run-times is fixed by the total length of the wire and does not depend on the position of impact. This poses a condition on the two run-time signals that makes it possible to reconstruct the correct pairs of run-times. It is therefore possible to identify the positions even if a second particles impact the delayline anode while the signals of a previous particle are still propagating.

## 3.2 FLASH

This overview of the Free-Electron Laser in Hamburg (FLASH and FLASH2) summarises its characteristic properties and is mostly compiled from DESY (2017a) and Schmüser, Dohlus, and Rossbach (2008).

The Free-Electron Laser in Hamburg (FLASH) at Deutsches Elektronen-Synchrotron (DESY) consists of one linear accelerator and two separate planar undulators as shown in Fig. 14. Originally, the linear accelerator had been constructed to investigate the technology of particle acceleration with superconducting cavities. The accelerator consists of seven 12 m long modules each containing eight niobium cavities cooled to 2 K to achieve superconductivity. Later, an undulator consisting of NdFeB permanent magnets was added to the accelerator which back then became the FLASH facility. In early 2000 the first ultraviolet FEL light was created by FLASH (Schmüser, Dohlus, and Rossbach, 2008, Ch. 8.1) and user operation started in August 2005. The FEL was later extended and equipped with a second undulator in a separate branch which became the FLASH2 facility. It offers additional available space for user experiments in a dedicated FLASH2 hall and a broader wavelength range of 4 to 90 nm as well as increased laser pulse energy.

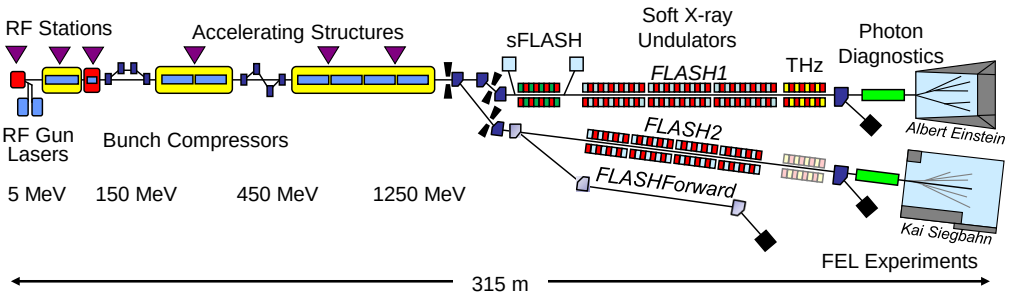


Figure 14: Schematic layout of FLASH with the two undulator sections (lower branch belongs to FLASH II). From DESY, 2017b.

The undulator of the FLASH2 branch consists of twelve modules each 2.5 m in length. They can be independently activated to increase the FEL radiation power up to and into saturation mode. The accelerator can provide electron bunch trains with a repetition rate of 10 Hz. The bunch trains can be adjusted to have a fixed number of individual bunches between one and several hundred. The undulator modules are arranged in a way that they create a magnetic field perpendicular to the ground. The electrons' sinusoidal path as well as the polarisation of the FEL radiation is therefore parallel to the ground. The undulator has a period of $\lambda_u = 31.4\,\mathrm{mm}$ with a peak magnetic field of 0.48 T. A new feature of the FLASH2 undulator compared to FLASH is the variable gap. It allows for quick tuning of the wavelength without influencing the FEL radiation with respect to FLASH. By varying the distance of the undulator magnets to the electron beam, the magnetic field inside the undulator is adjusted. This affects the undulator parameter $K$ (see Eqn. 4) and therefore the wavelength of the FEL radiation without having to change the electrons' energy. This way the wavelength of the FEL can be tuned to a desired value within seconds upon user request. Due to the structure of the undulators and the fixed electron beam energy for FLASH and FLASH2, it is only possible to vary the wavelength of FLASH2 by a factor of three relative to FLASH.

# 4 Results on XUV Pulse Length Measurements by Autocorrelation

## 4.1 Description of Data Set

The data analysed during this work was collected during beamtimes at FLASH2 in June 2016, October 2016, and February 2017. Each beamtime was separated into several shifts of one or more days. Each shift required a new tuning of the FEL and sometimes the FEL needed re-tuning during one shift. Periods of constant FEL parameters (wavelength, pulse energy, filters etc.) are called runs. One objective of measuring the pulse duration is to check whether it varies during measurements with one FEL tuning state. To answer this question, the pulse duration has been measured for consecutive runs taken during the same FEL tuning.

In total, 27 runs were analysed for autocorrelation signals in $Ne^{2+}$, $Ar^{2+}$, and $Ar^{4+}$ ion count rates. The runs were chosen mainly for their long measurement time since the autocorrelation signal usually takes several hours to be of statistical significance. The shortest run for which an autocorrelation signal was detected had a duration of approximately two hours. An overview of the analysed runs with some major measurement parameters is shown in Tab. 1.

The number of bunches per bunch train was highest for the $Ar^{4+}$ measurements (92 and 93), lower for the $Ne^{2+}$ runs (50) and lowest for the $Ar^{2+}$ beamtime (30 and 35). The bunch charge decreased with increasing number of bunches from 0.14 to 0.10 nC. The bunch repetition rate was 201 kHz for $Ne^{2+}$ and $Ar^{2+}$ and 100 kHz for $Ar^{4+}$. Changes in pulse energy (9.5 µJ to 74.6 µJ), aperture diameters (2 mm to 14 mm), MCP detector voltage, and FEL filter configurations were documented in an external file for future reference.

| run | total ion counts | scanned delay range [fs] | calibrated wavelength [nm] | features of autocorrelation signal |
|---|---|---|---|---|
| **$Ne^{2+}$** | | | | |
| R698 | 43 605 | 1200 | 46.36 | sharp spike, almost no base |
| R712 | 169 411 | 300 | 45.76 | sharp spike, low base |
| R713 | 7304 | 300 | 45.16 | no features |
| R724 | 201 778 | 300 | 46.16 | sharp spike, almost no base |
| R725 | 139 780 | 300 | 45.96 | sharp spike, broad base |
| R726 | 56 065 | 300 | 46.06 | sharp spike, broad base |
| R728 | 72 845 | 300 | 45.86 | sharp spike, broad base |
| R729 | 13 435 | 300 | 46.56 | low broad spike, no base, noisy |
| R730 | 2632 | 300 | 45.16 | no features |
| R731 | 6625 | 300 | 45.86 | low spike, no base, noisy |
| R732 | 45 814 | 300 | 46.21 | sharp spike, very broad base |
| R733 | 3250 | 300 | 45.51 | no features |
| R734 | 747 | 300 | 46.56 | no features |
| R736 | 718 | 300 | 45.86 | no features |
| **$Ar^{2+}$** | | | | |
| R740 | 33 944 | 666 | 51.76 | low spike, inverted base |
| R741 | 30 548 | 200 | 51.76 | spike, inverted base |
| R743 | 51 960 | 66 | 52.26 | spike, no base |
| R744 | 168 055 | 400 | 51.26 | no features |
| R745 | 34 879 | 400 | 51.16 | sharp spike, broad base |
| R746 | 2670 | 400 | 50.56 | high wide spike, narrow base |
| R748 | 379 | 400 | 52.26 | single high broad feature, noisy |
| R749 | 8936 | 400 | 51.76 | wide spike, high broad base |
| R750 | 159 073 | 400 | 50.76 | low spike, broad base |
| **$Ar^{4+}$** | | | | |
| R827 | 543 | 600 | 53.66 | sharp spike, very low base |
| R832 | 210 | 600 | 53.66 | narrow spike, noisy |
| R836 | 1786 | 600 | 52.36 | sharp spike, broad base |
| R837 | 4893 | 200 | 51.96 | sharp spike, broad base |

Table 1: Overview of the analysed runs. The delay was scanned symmetrically around zero. The horizontal lines separate the three beamtimes as well as the ion species corresponding to the analysed autocorrelation signal ($Ne^{2+}$, $Ar^{2+}$, and $Ar^{4+}$).

## 4.2 Time-of-Flight Spectra and Identification of Ion Species

The stored data files were loaded and unpacked in the software Go4 (GSI, 2017). In order to obtain the counts of the respective ion species depending on the delay between pump and probe pulses, a time-of-flight (TOF) condition was applied to filter the MCP signals. In some runs the detector received too many simultaneous hits to give meaningful position data. If positions could be measured, a position condition on the area where the ions originating from the target hit the detector showed almost no reduction in the number of ion counts. This shows that the background rate of noble gas ions other than from the target is very small.

Adjusting the correct TOF condition was done via the overall TOF histogram (see Fig. 15 and Fig. 16). It displays the detected counts over the time that passed between the FEL pulse hitting the target jet and the ion creating the signal on the detector. This total TOF spectrum is a superposition of the individual TOF spectra for every single FEL pulse that interacted with the target during the time of the entire run. Scattering light reflected from chamber walls, apertures and the back-reflecting split mirror is visible at small TOF values. At later TOFs differently structured signals appear that are created by ions from the background gas in the main chamber (e.g. $H_2{}^+$, $N_2{}^+$ and $H_2O^+$) and from the target jet. Because of the precise localisation of the jet in the main chamber and the low temperature of the target gas, the TOF of each target ion species is well defined and appears as a sharp spike in the TOF spectrum. By applying a TOF condition to the spikes and checking the positions corresponding to these MCP hits, one can verify that the particles causing the spikes originate almost exclusively from the target jet.

The time that an object which is initially at rest needs to travel a distance $s$ under constant acceleration $a$ is $t = \sqrt{2s/a}$. In case of a REMI, the acceler-

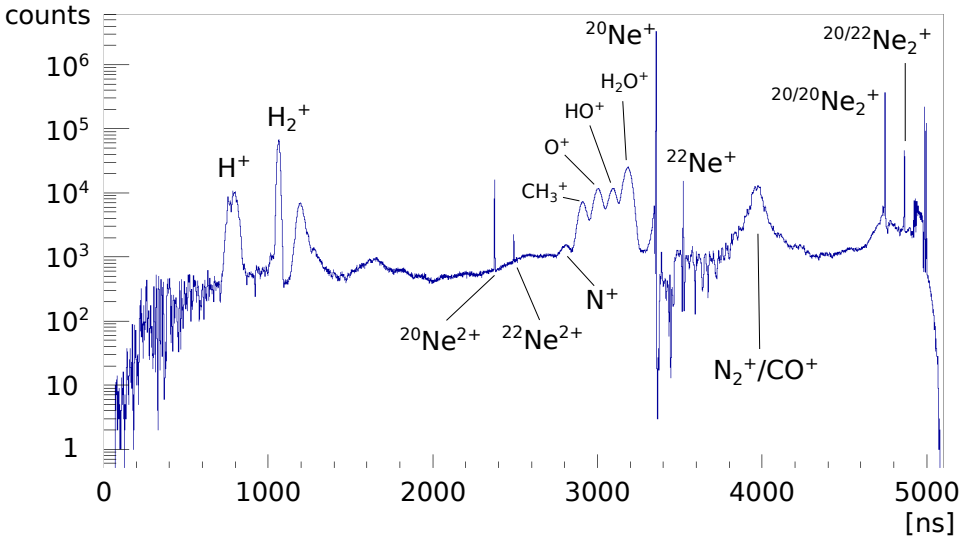


Figure 15: Example of a time-of-flight spectrum with neon target (run 698, photon energy 26.76 eV, pulse energy 44.0 µJ). At large time-of-flight values, signals of two types of neon dimers can be seen.

ation of the ions is caused by the electric field created by the spectrometer, $a = F/m = Eq/m$ where $q$ and $m$ are the charge and mass of the ion and $E$ is the electric field strength. Because the initial velocity of the atoms in the target jet is perpendicular to the electric field, the TOF is expressed by

$$t_{TOF} = \sqrt{\frac{2s}{E} \cdot \frac{m}{q}}. \tag{29}$$

It is proportional to the square root of the mass-to-charge ratio of an ion. Through this relation, individual ions can be identified in the TOF histogram. The twin lines at approximately 2367 ns and 2482 ns in Fig. 15 are caused by doubly ionised neon atoms of its two most abundant isotopes $^{20}$Ne (approx. 90 %) and $^{22}$Ne (approx. 9 %). At around $\sqrt{2}$ times their TOF values, the spikes of the two isotopes for singly ionised neon can be seen with $^{20}Ne^+$ having the highest peak of the entire spectrum. A sharp decrease in count rate is present following the $^{20}Ne^+$ peak which indicates that the detector operates in saturation. Indeed, the count rate of $^{20}Ne^+$ does not show any dependence

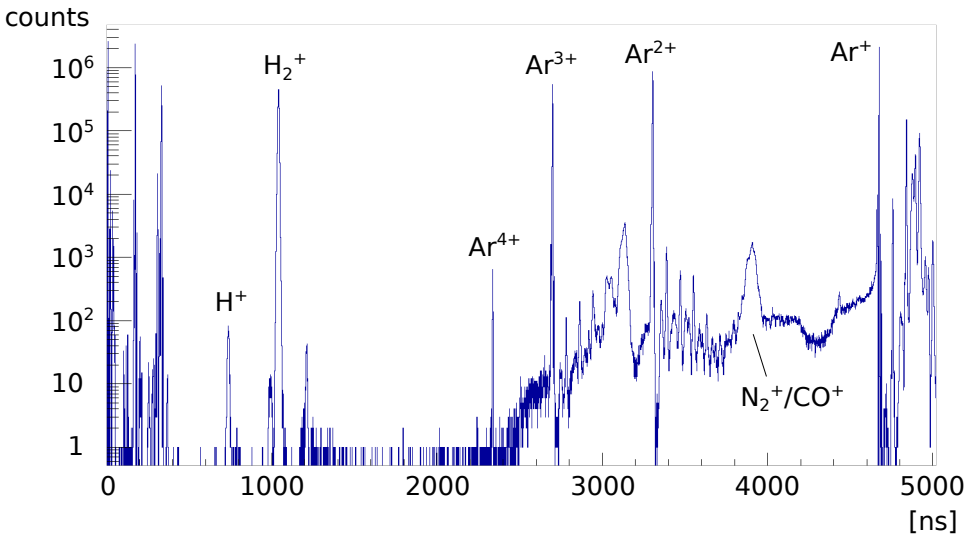


Figure 16: Example of a time-of-flight spectrum with argon target (run 836, photon energy 23.70 eV, pulse energy 36.7 µJ). Due to the high FEL intensity needed to ionise argon up to $Ar^{4+}$, the MCP is saturated which can be seen in the strong decline in detected counts immediately after the $Ar^+$, $Ar^{2+}$, and $Ar^{3+}$ peaks.

on the delay between pump and probe pulse, so it can be assumed that the $^{20}$Ne ionisation rate was saturated. This can also be observed in the TOF histogram in Fig. 16 where argon ions up to $Ar^{4+}$ were detected.

## 4.3 Wavelength Calibration

A wavelength calibration was done using the $Ar^+$ to $Ar^{2+}$ ionisation process. The FEL machine wavelength was varied in steps across the ionisation threshold of singly ionised argon (27.63 eV, 44.9 nm; NIST, 2017). The measured counts of $Ar^{2+}$ were normalised by the measured counts of the nitrogen background $N_2^+$ and plotted against the machine wavelength (see Fig. 17). The ratio is small for large wavelengths and increases strongly from 44.6 to 44.1 nm. Assuming the threshold lies in the middle of these two values, this leads to a machine wavelength of 44.35 nm for the ionisation

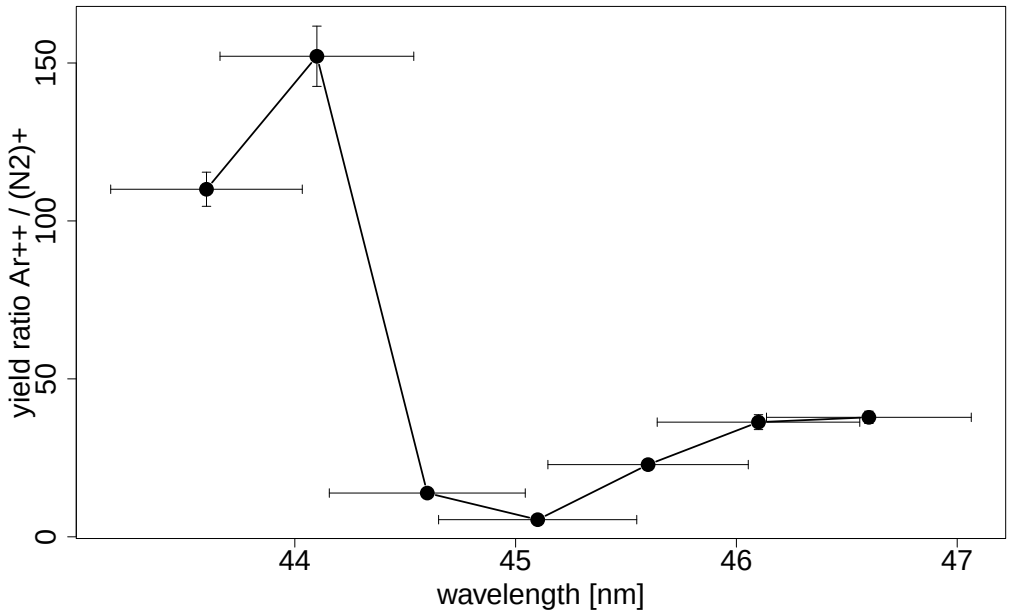


Figure 17: Ion yield ratio of $Ar^{2+}$ to $N_2{}^+$ used for wavelength calibration with the ionisation threshold of $Ar^+$ at 27.63 eV.

threshold. Therefore, the machine wavelength is 0.56 nm smaller compared to the wavelength expected from the literature, assuming a linear relation between them. This difference agrees well with wavelength measurements by the FLASH beam diagnostics monochromator (DESY, 2017a) which determined the actual wavelength to be 0.3 to 0.6 nm smaller compared to the machine wavelength. The actual wavelength is therefore calculated by subtracting 0.56 nm from the machine wavelength. The error in wavelength originates from the spectral bandwidth of the FEL which has been measured by Kuhlmann (2017) to be 0.44 nm FWHM (0.19 nm standard deviation) at 46 nm.

## 4.4 Autocorrelation Histograms

In the next step of the analysis, a histogram is created for each run showing the delay value between the pump and probe pulse on the x-axis and the number of ion counts in a specific TOF range on the y-axis. These histograms, called autocorrelation histograms, were exported from Go4 for each run for further analysis. The TOF condition was adjusted to the $^{20}Ne^{2+}$ peak for the June 2016 beamtime, to $Ar^{2+}$ for October 2016 and to $Ar^{4+}$ for February 2017 (see Fig. 16). When conducting a pump-probe measurement one cannot assure that the delay scan is started and stopped at the same mirror position. Therefore, some delay values may be scanned up to two times more often than others. To account for this, the ion counts from the autocorrelation histogram are divided by the respective value in the delay value histogram which represents the number of times the respective delay value has been scanned. The resulting normalised autocorrelation histogram is then scaled by the mean value of the delay value histogram. After exporting the raw data from Go4, the data was further processed using the programming language R.

## 4.5 Categorisation of Runs

Of the 27 analysed runs, six showed almost no features but only a rather noisy plateau where the ion count rate does not seem to vary with the delay. In Fig. 18a, the only $Ar^{2+}$ run without features is shown. The missing features could be related to the low pulse energy of only 8.6 µJ during that run. The other five runs without features are from $Ne^{2+}$ and have a low number of total ion counts which may be the reason for the absence of features in their autocorrelation histograms. Of the runs that show features, their prominence varies between the runs, as shown in Fig. 18b and Fig. 18c. Here, again, a different total number of ion counts could be responsible.

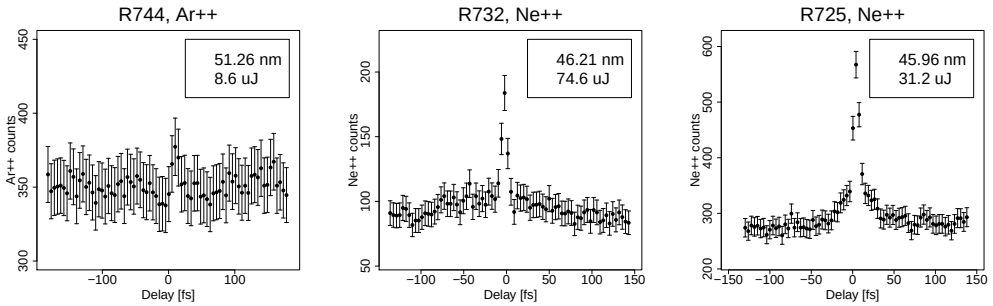


(a) (b) (c)

Figure 18: Examples of different autocorrelation signals. The left is from an $Ar^{2+}$ run at low pulse energy and shows almost no features. The other two are from $Ne^{2+}$ at different FEL wavelengths and pulse energies. The base feature is much more prominent in the histogram on the right compared to the one in the centre.

## 4.6 Determination of Average Pulse Duration

As mentioned in Section 2.3.1, the autocorrelation of a Gaussian pulse has as well a Gaussian shape with modified standard deviation and scale. The autocorrelation histograms were fitted with a nonlinear least squares function of the sum of two Gaussians relating the measured counts $N$ with the delay value $\delta$:

$$N(\delta) = A + C_1 \exp\left(-\frac{(\delta - \mu_1)^2}{2V_1}\right) + C_2 \exp\left(-\frac{(\delta - \mu_2)^2}{2V_2}\right). \qquad (30)$$

Here, $A$ is the offset, $C_1$ and $C_2$ are scaling factors of the two respective Gaussians, $\mu_1$ and $\mu_2$ are their mean values and $V_1$ and $V_2$ their variances. This fit function does not converge on all of the obtained autocorrelation histograms, especially not on the ones where the described features are barely recognisable. For the runs where the fit converges, the fit parameters were extracted including their standard errors. From the variance (the square of the standard deviation) of the Gaussian function that converged around the broad base structure, first the standard deviation of the original FEL pulse intensity profile $\sigma_p$ was calculated. For the two-photon ionisation processes

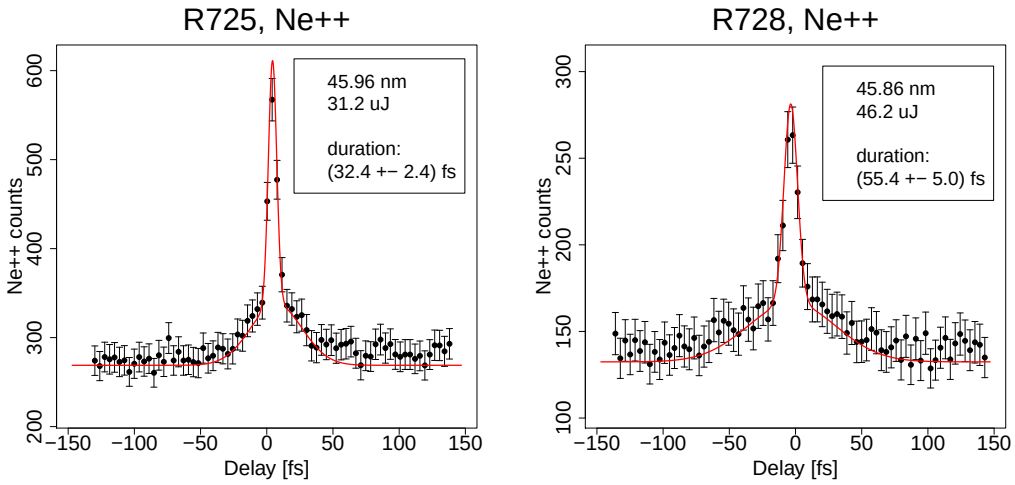


(a) (b)

Figure 19: Autocorrelation signals measured during runs 725 (left) and 728 (right) in doubly ionised neon. Red line is a double Gaussian fit.

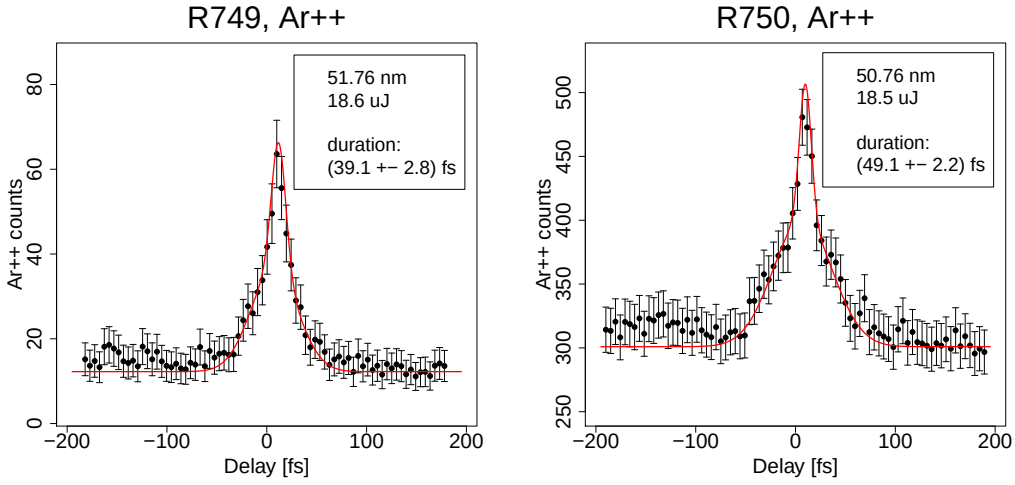


(a) (b)

Figure 20: Autocorrelation signals measured during runs 749 (left) and 750 (right) in doubly ionised argon. Red line is a double Gaussian fit.

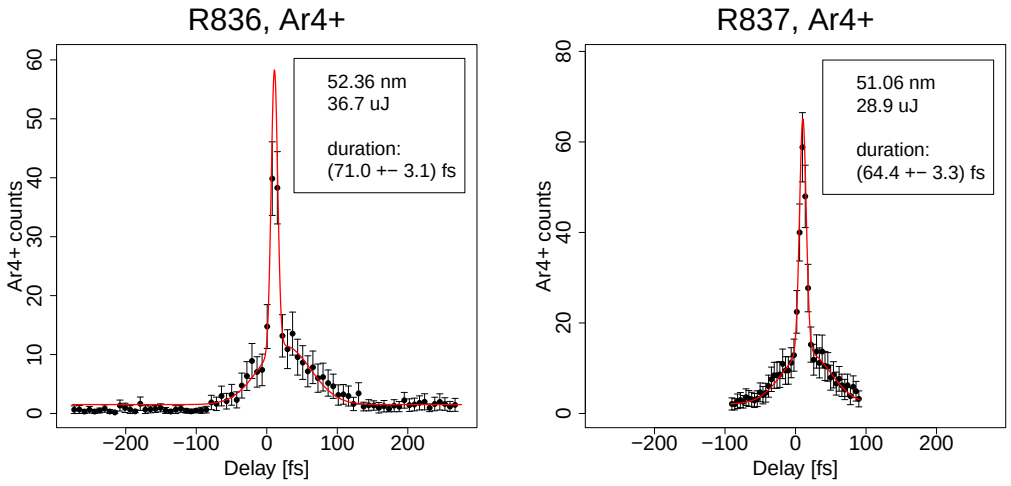


(a) (b)

Figure 21: Autocorrelation signals measured during runs 836 (left) and 837 (right) in quadruply ionised argon. Red line is a double Gaussian fit.

($Ne^+$ to $Ne^{2+}$ and $Ar^+$ to $Ar^{2+}$), Eqn. 20 was used: $\sigma_p = \sigma_{ac,2}/\sqrt{2}$. The conversion for the three-photon process from $Ar^{3+}$ to $Ar^{4+}$ was done according to Eqn. 21: $\sigma_p = \sigma_{ac,3}\sqrt{\frac{2}{3}}$. Then, with Eqn. 25 the average FWHM of the Gaussian-shaped intensity profile of the FEL pulses were calculated: $\mathrm{FWHM} = 2\sqrt{2\ln(2)}\ \sigma_p$. The obtained FWHM for the different runs with their standard errors are listed in Tab. 2. In Fig. 19 to Fig. 21, examples of the measured autocorrelation signals in the three different ion species are shown with their respective fit functions.

It can be seen that the autocorrelation signals detected during the three beamtimes vary in shape. For example, the height of the base feature compared to the coherence spike is much greater for the $Ar^{2+}$ ion counts compared to the other measurements. The autocorrelation histograms were measured with different values for wavelength and pulse energy. In order to find possible correlations between the autocorrelation features and the FEL wavelength and pulse energy, Fig. 22 to Fig. 25 have been prepared. Fig. 22 shows the measured FEL pulse length depending on the respective wavelength and pulse

energy during the run. The colours represent the different ion species. The same symbol shapes of each colour represent a specific state of FEL tuning.

As it can be seen from Fig. 22a, the neon runs were taken at lower wavelengths than the argon runs. While the pulse length for the neon measurements varies between 32.4 fs and 92.6 fs, the argon runs show a more narrow range of pulse lengths from 39.1 fs to 66.5 fs. In general, no dependence of the FEL pulse length on the wavelength is evident from the collected data.

In Fig. 22b, where the pulse duration and the respective pulse energies are shown, short pulses occur at lower energies. Pulse durations at energies above 40 µJ are longer compared to most measured pulse durations at lower energies. This appears plausible since a higher pulse energy is acquired by longer electron bunches. One method of checking this relation is by plotting the electron bunch charge over the pulse energy for all runs as shown in Fig. 23. The argon measurements were mostly done with lower electron bunch charge compared to the neon runs. Together with the observation that on average shorter FEL pulses were measured in the argon measurements, this supports the connection of higher bunch charges causing higher pulse energies which in turn create longer FEL pulses. More data, especially in the high energy range above 40 µJ is desirable to further investigate this correlation.

The width of the coherence spike in the autocorrelation signals seems to depend on the FEL wavelength as it can be seen in Fig. 24b. The argon measurements at higher wavelengths show an on average wider coherence features than the neon measurements at lower wavelengths. This seems plausible since the coherence of an FEL pulse is connected to the width of the spikes in its intensity profile. These spikes originate from coherently radiating electron microbunches (see Section 2.1) which are separated by approximately one wavelength. If the wavelength is shorter, the microbunches are closer together and the length of the coherent intensity spikes is shorter. When

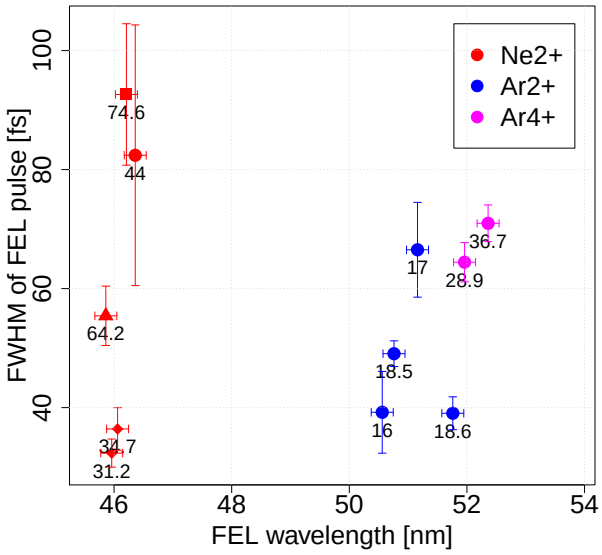


(a)

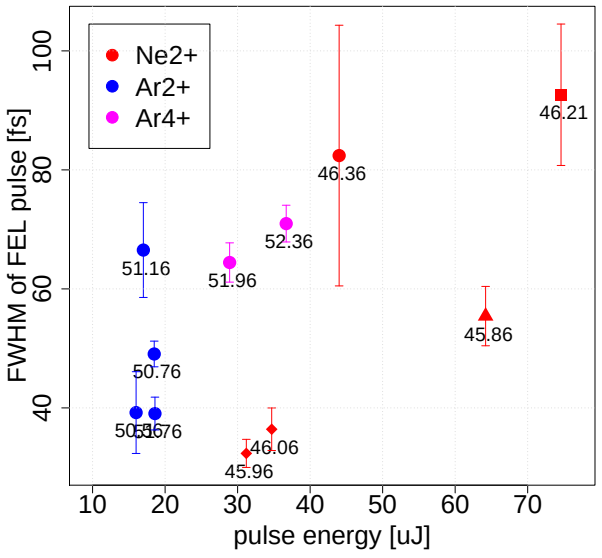


(b)

Figure 22: Pulse duration plotted against FEL wavelength (a) and pulse energy (b). The labels designate the pulse energy in µJ (a) and the FEL wavelength in nm (b), respectively. Equal symbol shapes represent equal FEL tuning states for each colour separately.

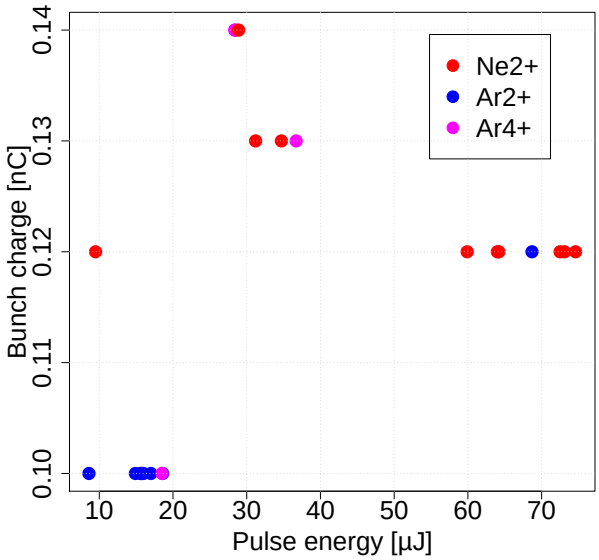


Figure 23: Electron bunch charge over pulse energy. The bunch charge was on average lower during the argon measurements which resulted in shorter FEL pulses (see Fig. 22b.

examining the coherence spike depending on the pulse energy (see Fig. 24b), no correlation appears to be evident other than a lack of wide coherence spikes for high energies.
When plotting the average FEL pulse length over the width of the coherence spike as in Fig. 25, no obvious general correlation can be seen. The $Ar^{2+}$ measurements tend to have a larger spike width at on average shorter pulses while the $Ar^{4+}$ and $Ne^{2+}$ runs show a wide range of pulse lengths with on average more narrow coherence spikes.

For the neon measurements the ionisation process from $Ne^{+}$ to $Ne^{2+}$ is of special interest because of the $2p - 3s$ resonance at 45.6 nm. At larger wavelengths the sequential two-photon ionisation path is blocked because the photon energy is too low to excite the resonant state. Therefore, only the delay-dependent direct path contributes to the $Ne^{2+}$ ion count rate and a stronger autocorrelation signal is expected.

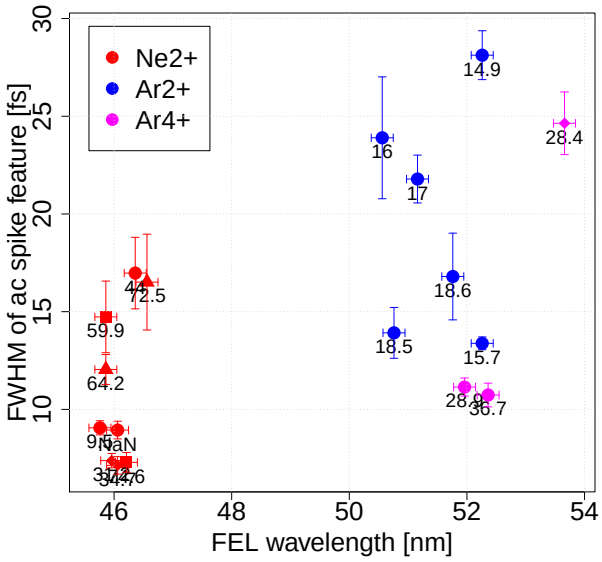


(a)

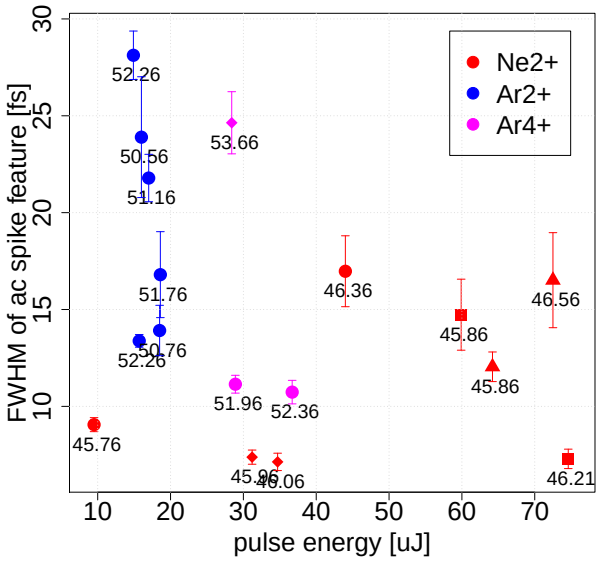


(b)

Figure 24: FWHM of coherence spike feature plotted against FEL wavelength (a) and pulse energy (b). The labels designate the pulse energy in µJ (a) and the FEL wavelength in nm (b), respectively. Equal symbol shapes represent equal FEL tuning states for each colour separately.

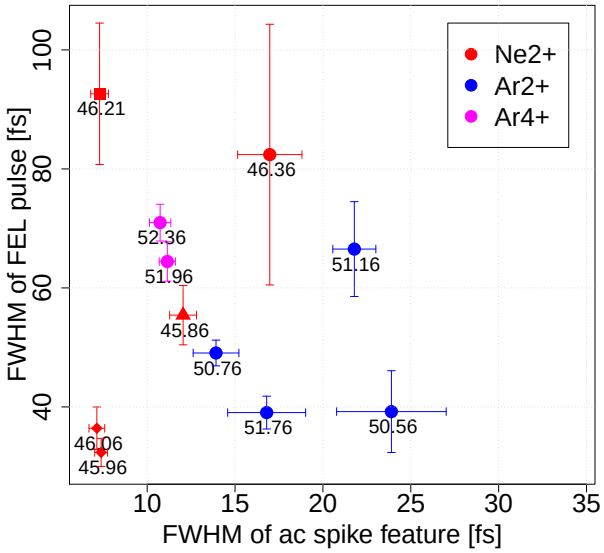


Figure 25: FEL pulse duration plotted against width of coherence spike. The labels designate the FEL wavelength in nm. Equal symbol shapes represent equal FEL tuning states for each colour separately.

When checking the wavelength-dependence of the autocorrelation features in Tab. 1, five neon runs did not show any features in their histograms. Three of them were recorded at photon energies sufficiently high enough to reach the resonant state. The other neon runs were taken at wavelengths larger than the resonance and show autocorrelation features of various degrees of prominence. The explanation for this could be that at high enough photon energies the resonant two-photon ionisation process dominates. Because the intermediate excited state has a long lifetime compared to the applied delay, the sequential ionisation path does not depend on the delay and therefore does not cause autocorrelation signals. However, all five neon runs without autocorrelation features have a very low total number of ion counts (718 to 3250) compared to approximately $10^4$ to $10^5$ ions in the other runs. If more data was collected and the ion counts increased, it is possible that autocorrelation features would have occurred.

| run | FWHM of coherence spike [fs] | average FWHM of FEL pulses [fs] |
|---|---|---|
| **$Ne^{2+}$** | | |
| R698 | $16.98 \pm 1.83$ | $82.41 \pm 21.90$ |
| R712 | $9.06 \pm 0.36$ | - |
| R724 | $8.94 \pm 0.45$ | - |
| R725 | $7.38 \pm 0.37$ | $32.36 \pm 2.36$ |
| R726 | $7.14 \pm 0.45$ | $36.41 \pm 3.58$ |
| R728 | $12.04 \pm 0.76$ | $55.43 \pm 4.99$ |
| R729 | $16.51 \pm 2.45$ | - |
| R731 | $14.73 \pm 1.83$ | - |
| R732 | $7.29 \pm 0.50$ | $92.63 \pm 11.88$ |
| **$Ar^{2+}$** | | |
| R743 | $13.38 \pm 0.33$ | - |
| R745 | $21.79 \pm 1.22$ | $66.53 \pm 7.97$ |
| R746 | $23.90 \pm 3.12$ | $39.21 \pm 6.87$ |
| R748 | $28.12 \pm 1.25$ | - |
| R749 | $16.80 \pm 2.22$ | $39.05 \pm 2.76$ |
| R750 | $13.92 \pm 1.30$ | $49.06 \pm 2.16$ |
| **$Ar^{4+}$** | | |
| R827 | $24.64 \pm 1.60$ | - |
| R836 | $10.74 \pm 0.61$ | $70.97 \pm 3.09$ |
| R837 | $11.14 \pm 0.46$ | $64.44 \pm 3.30$ |

Table 2: FWHM of coherence spike and pulse duration for each run. The fit did not converge around the base feature for runs 712, 724, 729, 731, 743, 748, and 827. For run 698 the delay range used for fitting had to be reduced by more than half for the fit to converge around the very weak base feature. The horizontal lines separate the three beamtimes as well as the ion species corresponding to the analysed autocorrelation signal ($Ne^{2+}$, $Ar^{2+}$, and $Ar^{4+}$).

# 5 Conclusion

For the first time since its start of operation in 2016, the FEL pulse durations of FLASH2 at DESY, Hamburg, have been measured. The obtained pulse durations between (32.4±2.4) fs and (92.6±11.9) fs proof that FLASH2 does in fact routinely deliver intense femtosecond light pulses in the extreme-ultraviolet regime. These results represent first benchmarks for future experiments.
The measurements applying of intensity autocorrelation were performed with the reaction microscope at the permanent user endstation of beamline FL26. Three different multiphoton ionisation processes have been used to acquire autocorrelation signals of second order (with $Ne^{2+}$ and $Ar^{2+}$ ion yields) and third order (with $Ar^{4+}$ ion yields). That way, intensity autocorrelation measurements have been shown to be a reliable direct method to measure pulse durations at FLASH2.

Correlations in the measured pulse durations with FEL parameters suggest that longer pulses occur at higher pulse energies. At the same time, higher pulse energies coincide with a higher electron bunch charge. This observation supports the connection that the electron bunch charge influences the bunch length which in turn affects the pulse duration.
The width of the coherence spike in the autocorrelation signals was found to be smaller for shorter wavelengths. This is expected since the partial coherence of the FEL radiation originates from coherently radiating electron microbunches which are separated by a distance on the order of the FEL wavelength.

A resonant excitation process in singly ionised neon may influence the measured autocorrelation signal. No autocorrelation signals were present when the FEL wavelength was sufficiently short to excite the resonant $2p - 3s$ transition in $Ne^{+}$. However, these measurements show a low total count rate of detected ions. Autocorrelation features may have emerged at longer

measurement times. An absence of autocorrelation features caused by a sequential resonant two-photon ionisation process are therefore not conclusively proven. However, until further knowledge is obtained on how exactly resonant states influence autocorrelation signals, one should avoid using photon energies which resonantly excite energy levels in the target during pulse duration measurements.

A good candidate for such a clean autocorrelation measurement is atomic helium. To ionise one of the two $1s$ electrons, an energy of 24.6 eV is needed (NIST, 2017). The first excited dipole-allowed state $1s2p$ lies at 21.0 eV. Hence, the possibility of FLASH2 to tune to photon energies as low as 14 eV allows to get an unperturbed autocorrelation signal in the non-sequential two-photon ionisation of helium.
Following this idea, a combined action including the accelerator machines' people would help to measure the FEL pulse duration in a more comprehensive and organised way by testing e.g. for different injector, accelerator, and undulator settings.

# A Autocorrelation of simulated Gaussian Intensity Profiles (R-Script)

```
1  # define a Gaussian functions
2
3  offset = 0
4  scale = 1
5  m = 0
6  sd = 3
7
8  g1 <- function(x){
9
10 return(offset+scale*exp(-(x-m)^2/(2*sd^2)))
11 }
12
13 # define discrete x-coordinate
14 # step size
15 dx = 0.2
16 # minimum of range
17 minRange = -15
18 # maximum of range
19 maxRange = 15
20
21 x = seq(minRange,maxRange,dx)
22
23 # define limits for plots
24 xlimit=c(min(x), max(x))
25 ylimit=c(0,8)
26
27 # define "noise" (factor in jitter() function)
28 noise = 50
29
30 # initialise arrays with zeros
31 a = seq(0,0,length=(maxRange-minRange)/dx)
32 b = seq(0,0,length=(maxRange-minRange)/dx)
33 s = seq(0,0,length=3*(maxRange-minRange)/dx)
34
35 for (k in 1:length(x))
36 {
37         s[-2*minRange/dx + k] = jitter(g1(x[k]),noise)
38 }
39
40
```

```
41 # autocorrelation
42 for (i in 1:length(x))
43 {
44         for (j in 1:length(x))
45         {
46                 # b is intermediate array
47                 b[j] = s[-2*minRange/dx+j]*s[-2*minRange/dx+j-x[
       i]/dx]
48         }
49         # a stores the autocorrelation signal
50         a[i] = sum(b)
51 }
52
53 a = a*dx
54
55 #plot to file
56 pdf("autocorr.pdf", height=8, width=8)
57
58 # plot original signal
59 plot(x,s[(-2*minRange/dx+1):(-2*minRange/dx+length(x))], xlab=""
       , ylab="", xlim=xlimit, ylim=ylimit, xaxt="n", yaxt="n", t="l
       ", lwd=2, col=8)
60
61 axis(1,cex.axis=1.2)
62 axis(2,cex.axis=1.2)
63 mtext("(delay) time arb. u.", side=1, line=3, cex=2)
64 mtext("intensity (autocorrelation signal) arb. u.", side=2, line
       =2.5, cex=2)
65
66 # plot autocorrelation
67 par(new=T)
68 plot(x,a, axes=F, xlim=xlimit, ylim=ylimit, xlab="", ylab="", t=
       "p", col=1)
69
70 # Gaussian model
71 dat=data.frame(x,a)
72 model=nls(a~(scale*exp(-(x)^2/(2*v))), data=dat, start=list(
       scale=5.0,v=19), trace=TRUE)
73
74 # store fit coefficients from Gaussian model
75 scale= coefficients(model)[1]
76 v=     coefficients(model)[2]
77
78
```

```
79 # calculate FWHM of original pulse from fit to aotocorrelation
80 FWHM = 2*sqrt(log(2)*v)
81
82 # draw curve of Gaussian model
83 par(new=T)
84 curve(scale*exp(-x^2/(2*v)), n=length(x)*10, xlim=xlimit, ylim=
       ylimit, xlab="", ylab="", axes=F, col=1, lwd=2, lty=2)
85
86 legend(maxRange*0.25, 8.5*0.95, paste("FWHM_p: ", format(FWHM,
       digits=4)), cex=1.5)
87
88 dev.off()
```

# Bibliography


[1] J. D. Bozek. "AMO instrumentation for the LCLS X-ray FEL". In: *Eur. Phys. J. Special Topics* 169 (2009), pp. 129–132.

[2] P. A. Bromiley. *Products and Convolutions of Gaussian Probability Density Functions*. Internal Report No. 2003-003. School of Medicine, University of Manchester. Aug. 2014.

[3] P. B. Corkum. "Plasma Perspective on Strong-Field Multiphoton Ionization". In: *Phys. Rev. Lett.* 71 (1993), pp. 1994–1997.

[4] W. Demtröder. *Experimentalphysik 3. Atome, Moleküle und Festkörper*. Springer-Verlag Berlin Heidelberg, 2009. ISBN: 978-3-642-03910-2.

[5] W. Demtröder. *Experimentalphysik 4. Kern-, Teilchen- und Astrophysik*. Springer-Verlag Berlin Heidelberg, 2009. ISBN: 978-3-642-01597-7.

[6] DESY. *Accelerator*. Feb. 2017. URL: `http://flash.desy.de/accelerator/`.

[7] DESY. *FLASH*. Feb. 2017. URL: `http://flash.desy.de/`.

[8] DESY. *FLASH Online Photoionization Spectrometer (OPIS)*. Mar. 2017. URL: `http://photon-science.desy.de/facilities/flash/photon_diagnostics/opis_spectrometer/index_eng.html`.

[9] A. L. Cavalieri *et al.* "Attosecond spectroscopy in condensed matter". In: *Nature* 449 (2007), pp. 1029–1032.

[10] A. Lutman *et al.* "Polarization control in an X-ray free-electron laser". In: *Nat. Photon.* 10 (2016), pp. 468–472.

[11] K. Schnorr *et al.* "Time-Resolved Measurement of Interatomic Coulombic Decay in $Ne_2$". In: *Phys. Rev. Lett.* 111 (2013), p. 093402.

[12] K. Zhao *et al.* "Tailoring a 67 attosecond pulse through advantageous phase-mismatch". In: *Opt. Lett.* 37.18 (2012), pp. 3891–3893.

[13] L. A. Lompre *et al.* "Multiphoton ionization of rare gases by a tunable-wavelength 30-psec laser pulse at 1.06 µm". In: *Phys. Rev. A* 15.4 (1977), pp. 1604–1612.

[14] M. LuVan *et al.* "Multiphoton Ionization of Atomic and Molecular Hydrogen at $0.53\,\mu$". In: *Phys. Rev. A* 7.1 (1973), pp. 91–98.

[15] P. Rudawski *et al.* "A high-flux high-order harmonic source". In: *Rev. Sci. Instrum.* 84.7 (2013), p. 073103.

[16] R. Moshammer *et al.* "A $4\pi$ recoil-ion electron momentum analyzer: a high-resolution "microscope" for the investigation of the dynamics of atomic, molecular and nuclear reactions". In: *Nuclear Instruments and Methods in Physics Research B* 108 (1996), pp. 425–445.

[17] R. Riedel *et al.* "Single-shot pulse duration monitor for extreme ultraviolet and X-ray free-electron lasers". In: *Nat. Comm.* 4.1731 (2013), pp. 1–7.

[18] R. W. Schoenlein *et al.* "Generation of Femtosecond Pulses of Synchrotron Radiation". In: *Science* 287 (2010), pp. 2237–2240.

[19] S. J. Goh *et al.* "Single-shot fluctuations in waveguided high-harmonic generation". In: *Optics Express* 23.19 (2015), pp. 24888–24902.

[20] T. Pfeifer *et al.* "Partial-coherence method to model experimental free-electron laser pulse statistics". In: *Opt. Lett.* 35.20 (2010), pp. 3441–3442.

[21] U. Frühling *et al.* "Single-shot terahertz-field-driven X-ray streak camera". In: *Nat. Photon.* 3 (2009), pp. 523–528.

[22] V. Ayvazyan *et al.* "First operation of a free-electron laser generating GW power radiation at 32 nm wavelength". In: *Eur. Phys. J. D* 37 (2006), pp. 297–303.

[23] T. Feigl. *optiXfab*. Personal communication. Mar. 15, 2017. URL: `http://www.optixfab.com/impressum.html`.

[24] FERMI. *Elettra and FERMI lightsources*. Mar. 2017. URL: `http://www.elettra.eu/lightsources/fermi/fermi-machine/general-description.html`.

[25] Y. Gontier and M. Trahin. "Multiphoton Processes in a Hydrogen Atom". In: *Phys. Rev. A* 4.5 (1971), pp. 1896–1906.

[26] Helmholtzzentrum für Schwerionenforschung GmbH GSI. *The Go4 Project Page*. Mar. 2017. URL: `http://go4.gsi.de`.

[27] I. V. Hertel and C.-P. Schulz. *Atoms, Molecules and Optical Physics 1. Atoms and Spectroscopy*. Springer-Verlag Berlin Heidelberg, 2015. ISBN: 978-3-642-54321-0.

[28] M. Kuhlmann. Personal communication. Feb. 27, 2017.

[29] H. Mashiko. "Focusing coherent soft-x-ray radiation to a micrometer spot size with an intensity of $10^{14}\,\mathrm{W/cm^2}$". In: *Opt. Lett.* 29.16 (2004), pp. 1927–1929.

[30] S. Meister. "XUV Free-Electron Laser Experiments on Weakly Bound Dimers: Construction of a Water-Dimer Jet Source and Resonance-Enhanced ICD oin $Ne_2$". MA thesis. Heidelberg University, 2016.

[31] National Institute of Standards and Technology NIST. *Atomic Spectra Database*. Mar. 2017. URL: `https://www.nist.gov/pml/atomic-spectra-database`.

[32] C. Pellegrini. "The physics of x-ray free-electron lasers". In: *Reviews of Modern Physics* 88 (2016), p. 015006.

[33] C. Pellegrini. "X-ray free-electron lasers: from dreams to reality". In: *Physica Scripta* T169 (2016), p. 014004.

[34] P. Schmüser, M. Dohlus, and J. Rossbach. *Ultraviolet and Soft X-Ray Free-Electron Lasers. Introduction to Physical Principles, Experimental Results, Technological Challenges*. Springer-Verlag Berlin Heidelberg, 2008. ISBN: 978-3-540-79571-1.

[35] K. Schnorr. "XUV Pump-Probe Experiments on Electron Rearrangement and Interatomic Coulombic Decay in Diatomic Molecules". PhD thesis. Heidelberg University, 2014.

[36] SwissFEL. *Press release, 05. December 2016*. Mar. 2017. URL: `https://www.psi.ch/media/der-swissfel-ist-eingeweiht`.

[37] European XFEL. *Press release, 27. January 2017*. Mar. 2017. URL: `http://www.xfel.eu/news/2017/great_expectations_at_last_users_meeting_before_start_of_operation/`.

[38] K. Yamanouchi and K. Midorikawa. "Multiphoton Processes and Attosecond Physics". In: Springer-Verlag Berlin Heidelberg, 2012. Chap. Characterization of extreme ultra-violet FEL pulses by autocorrelation.

# Acknowledgement

Now, at the end, I would like to thank everyone who contributed to the success of this work:

- my group members Kirsten, Georg, Severin, Hannes, Sven, and Yifan for their kind and helpful advice, the exciting beam times at FLASH2, and the great working environment.
- in particular Kirsten and Georg for patiently and tirelessly answering all my questions.
- Robert Moshammer and Thomas Pfeifer for their expertise and guidance.
- Andreas Wolf for teaching me many things about atomic physics.
- the people of FLASH2 for making every effort to provide a well-tuned FEL beam, especially Rolf Treusch, Bart Faatz, Marion Kuhlmann, Markus Braune, and many others.
- for proofreading this thesis: Daniel Rahner, Salomé Mielke, Tobias Sattler, and the people already mentioned.
- my brother, my parents, and my grandparents for their support and their wisdom.
- the German taxpayers for financing this exciting and important research.

# Erklärung

Hiermit versichere ich, dass ich diese Arbeit selbstständig verfasst habe und keine anderen als die angegebenen Quellen und Hilfsmittel verwendet habe.